Particle Size Estimation in Ice-Phase Clouds Using Multifrequency Radar Reflectivity Measurements at 95, 33, and 2.8 GHz

STEPHEN M. SEKELSKY

Microwave Remote Sensing Laboratory, University of Massachusetts—Amherst, Amherst, Massachusetts

WARNER L. ECKLUND

Cooperative Institute for Research in Environmental Sciences, University of Colorado, Boulder, Colorado

JOHN M. FIRDA

Microwave Remote Sensing Laboratory, University of Massachusetts—Amherst, Amherst, Massachusetts

KENNETH S. GAGE

NOAA Aeronomy Laboratory, Boulder, Colorado

ROBERT E. MCINTOSH

Microwave Remote Sensing Laboratory, University of Massachusetts—Amherst, Amherst, Massachusetts

(Manuscript received 4 June 1997, in final form 20 April 1998)

ABSTRACT

Multifrequency radar measurements collected at 2.8 (S band), 33.12 (Ka band), and 94.92 GHz (W band) are processed using a neural network to estimate median particle size and peak number concentration in ice-phase clouds composed of dry crystals or aggregates. The model data used to train the neural network assume a gamma particle size distribution function and a size–density relationship having decreasing density with size. Results for the available frequency combinations show sensitivity to particle size for distributions with median volume diameters greater than approximately 0.2 mm.

Measurements are presented from the Maritime Continent Thunderstorm Experiment, which was held near Darwin, Australia, during November and December 1995. The University of Massachusetts—Amherst 33.12/94.92-GHz Cloud Profiling Radar System, the NOAA 2.8-GHz profiler, and other sensors were clustered near the village of Garden Point, Melville Island, where numerous convective storms were observed. Attenuation losses by the NOAA radar signal are small over the pathlengths considered so the cloud-top reflectivity values at 2.8 GHz are used to remove propagation path losses from the higher-frequency measurements. The 2.8-GHz measurements also permit estimation of larger particle diameters than is possible using only 33.12 and 94.92 GHz. The results suggest that the median particle size tends to decrease with height for stratiform cloud cases. However, this trend is not observed for convective cloud cases where measurements indicate that large particles can exist even near the cloud top.

1. Introduction

Multiple-wavelength radars have demonstrated the ability to estimate effective hydrometeor size in various forms of precipitation (Eccles and Atlas 1973; Lhermitte 1987; Matrosov 1992; Sekelsky and McIntosh 1996). Quantitative estimates of particle size are retrieved from differences in equivalent radar reflectivity Z_e measured at the different wavelength pairs using the dual-wavelength ratio (DWR), which is defined as

$$\mathrm{DWR}_{l,h} = 10 \log\left(\frac{Z_{e,l}}{Z_{e,h}}\right), \quad (1)$$

where l denotes the lower-frequency radar band and h denotes the higher-frequency radar band. Equivalent radar reflectivity is given by

$$Z_e = \frac{10^{12}\lambda^4}{4\pi^4}|K_w(\lambda)|^{-2} \int_0^\infty \xi_b(D, \lambda, \rho)D^2N(D)\, dD, \quad (2)$$

Corresponding author address: Stephen M. Sekelsky, Dept. of Electrical and Computer Engineering, Knowles 209 C, University of Massachusetts, Amherst, MA 01003.
E-mail: sekelsky@mirsl.ecs.umass.edu

where Z_e is used instead of Z to indicate the possibility of non-Rayleigh scattering and has units of $mm^6\ m^{-3}$. Note that the dynamic range of the observed reflectivity values is large so reflectivity is often expressed as dBZ_e, where $dBZ_e = 10\log(Z_e)$. The backscatter efficiency ξ_b is a function of particle diameter D [mm]; radar wavelength λ [m]; particle density ρ [g cm^{-3}]; and particle shape, which is discussed in a later section. Here, N [$mm^{-1}\ m^{-3}$] is the particle number density. The dimensionless quantity K is given as $K = \{[n(\lambda, \rho)^2 - 1]/[n(\lambda, \rho)^2 + 2]\}$, where n is the complex index of refraction. Because the true index of refraction for the media observed is typically unknown, $|K|^2$ is assumed to be that for liquid water $|K_w|^2$ at 0°C, which is typically 0.93 at low frequencies. Values of $|K|^2$ for water and solid ice are given in Table 1 for the frequencies of interest in this study. Because $|K_w|^2$ is not constant with frequency DWR, as defined in Eq. (1), we will have slightly negative values for small diameter particles. DWR is defined in this manner to make clear the assumptions that Z_e is calculated with respect to a specific dielectric constant.

DWR is primarily a function of particle size, while Z_e has a more complex dependence upon particle size, number density, and dielectric constant or density. Below we assume that $N(D)$ is the gamma distribution $N(D) = N_o D^\mu \exp[-(3.67 + \mu)D/D_o]$, as described by Ulbrich (1983). Using this relationship, (2) and (1) reduce to

$$Z_e = \frac{10^{12}\lambda^4}{4\pi^4}|K_w(\lambda)|^{-2}N_o \times \int_0^\infty \xi_b(D, \lambda, \rho)D^{2+\mu}\exp[-(3.67 + \mu)D/D_o]\,dD, \tag{3}$$

and,

$$\mathrm{DWR}_{l,h} = 10\log\left(\frac{\lambda_l^4|K_w(\lambda_h)|^2\int_0^\infty \xi_b(D, \lambda_l, \rho)D^{2+\mu}\exp[-(3.67 + \mu)D/D_o]\,dD}{\lambda_h^4|K_w(\lambda_l)|^2\int_0^\infty \xi_b(D, \lambda_h, \rho)D^{2+\mu}\exp[-(3.67 + \mu)D/D_o]\,dD}\right). \tag{4}$$

TABLE 1. Here, $|K_w|^2$ for water at 0°C and $|K_i|^2$ for solid ice are given for several radar bands. The last row shows the ratio of these two quantities that is used to convert between ice equivalent reflectivity and water equivalent reflectivity according to Eq. (20).

	W band (95 GHz)	Ka band (33 GHz)	S band (2.8 GHz)
$\lvert K_w\rvert^2$	0.698	0.885	0.934
$\lvert K_i\rvert^2$	0.176	0.176	0.176
$10\log(\lvert K_w\rvert^2/\lvert K_i\rvert^2)$	5.98 dB	7.01 dB	7.25 dB

Here, Z_e is a function of several variables, including N_o [$mm^{-1-\mu}\ m^{-3}$]. Aside from the wavelength pair selected, DWR depends upon D_o [mm], μ, and ρ [g cm^{-3}]. We will later show that DWR is fairly insensitive to density when ρ decreases with D. We also show that $\mathrm{DWR}_{\mathrm{Ka,W}}$ and $\mathrm{DWR}_{\mathrm{S,W}}$ are insensitive to μ for $D_o < 2$ mm and that $\mathrm{DWR}_{\mathrm{S,Ka}}$ is fairly insensitive to μ for values of D_o up to 10 mm. Therefore, D_o is obtained from DWR. If reasonable assumptions are made for $\rho(D)$ and μ (see section 3), then N_o can also be determined from Z_e.

Multifrequency particle sizing works when the higher-frequency experiences non-Rayleigh or Mie scattering. For cloud particle sizing, the higher frequency must exhibit non-Rayleigh scattering from small hydrometeors. For ice crystals this occurs at millimeter wavelengths where radar systems typically operate in one of several atmospheric transmission windows centered near 35, 95, 140, and 215 GHz. Radar–lidar and other techniques can detect smaller particle diameters in cirrus clouds and are superior to multifrequency radar in cold cirrus clouds where median diameters can be tens of microns. However, lidar signals are attenuated by low-level liquid clouds and are of limited use in optically thick clouds or during precipitation.

Although the minimum size that can be inferred from DWR is determined by the wavelength of the higher-frequency signal, atmospheric extinction increases with frequency and scattering losses from ice aggregates at 140 and 215 GHz can be substantial, even for dry ice particles (Nemarich et al. 1984). The choice of lower frequency is a trade-off between the maximum particle size that can be detected and system portability. As wavelength increases, the antenna diameter must also increase to maintain spatial resolution and sensitivity to clouds.

Multifrequency observations of precipitation and ice clouds measured by the University of Massachusetts—Amherst 33/95-GHz Cloud Profiling Radar System (CPRS) are reported by Sekelsky and McIntosh (1996). However, attenuation at these frequencies is still problematic in cases where the effects of non-Rayleigh scattering and attenuation cannot be separated with a high

TABLE 2. One-way extinction rates as a function of frequency calculated for rain using a Marshall–Palmer (1948) drop size distribution and an exponential distribution for snow described by Gunn and Marshall (1958).

Precipitation rate (mm h^{-1})	W band $K_{e,W}$ (dB km^{-1})	Ka band $K_{e,Ka}$ (dB km^{-1})	S band $K_{e,S}$ (dB km^{-1})
Rain			
0.1	0.1	9.4×10^{-3}	2.8×10^{-5}
1.0	1.0	0.14	2.1×10^{-4}
10.0	6.2	1.7	1.7×10^{-3}
Dry snow			
0.1	1.1×10^{-3}	3.8×10^{-4}	2.1×10^{-5}
1.0	2.3×10^{-2}	7.7×10^{-3}	2.1×10^{-4}

TABLE 3. Summary of MCTEX water vapor and oxygen absorption measurements from combined radiosonde, dual-channel radiometer, and surface observations. The mean surface humidity measured at Garden Point, Melville Island, is 19.9 g m^{-3} and the mean water vapor path is 4.98 cm. Zenith absorption is calculated by integrating the absorption rate from the surface to a height of 15 km.

	W band (95 GHz)	Ka band (33 GHz)	S band (2.8 GHz)
Average surface level absorption rate (dB km^{-1})	1.36	0.22	0.005
Average two-way zenith absorption (dB)	5.9	1.1	0.06

degree of confidence, such as when precipitation and melting particles are present in the propagation path. By combining CPRS measurements and those collected with the nonattenuating National Oceanic and Atmospheric Administration (NOAA) Aeronomy Laboratory S-band (2.8 GHz) radar, these uncertainties are better resolved and more accurate estimates of particle size distributions are possible. Table 2 compares extinction rates for the three frequencies considered in rain and snow, and Table 3 lists typical absorption rates for the humid tropical atmosphere. We see that S-band attenuation can be ignored for the zenith measurements considered in this paper.

The following sections describe the University of Massachusetts—Amherst (UMass) and NOAA radar hardware, scattering models for dry ice crystals and aggregates, and the neural network methodology that processes the multifrequency measurements. Finally, neural network outputs are presented for data collected during the Maritime Continent Thunderstorm Experiment (MCTEX).

2. Radar hardware

a. UMass Cloud Profiling Radar System

CPRS consists of 94.92 (W band) and 33.12 GHz (Ka band) subsystems, a programmable pedestal that facilitates various scanning modes and a high-speed VXI-bus-based data acquisition and digital signal processing (DSP) system (Sekelsky and McIntosh 1996; Lohmeier et al. 1997). Both the 33- and 95-GHz subsystems transmit and receive through a single 1-m-diameter dielectric lens antenna. The use of a single aperture eliminates pointing errors between the two frequencies and the lens acts as a radome protecting the hardware from precipitation. Other system characteristics are listed in Table 4.

Although CPRS is normally mounted on a truck, it was repackaged for operation from the standard 20-ft-length sea container shown in Fig. 1a, which is convenient for shipping and serves as a field laboratory. The microwave hardware is modular, and the antenna and radar front-ends sit outside the container atop an elevation-over-azimuth pedestal. Radar control and data acquisition for both CPRS and the NOAA radar, described below, are contained inside the air-conditioned sea container.

b. NOAA S-band profiler

The NOAA S-band radar shown in Fig. 1b operates at 2.835 GHz and uses a vertical-pointing shrouded parabolic reflector antenna, a simple and reliable solid-state transmitter, and much of the same hardware and software that is used in Aeronomy Laboratory 915-MHz profilers (Carter et al. 1995; Ecklund et al. 1999). The solid-state transmitter and associated electronics are mounted on the outside of the antenna shroud to minimize feed line loss. For the data presented in this paper, 130 Doppler spectra (128 points) were averaged from each of 60 heights during each 30-s time interval. The average spectra provide vertical Doppler velocity, signal-to-noise ratio, noise level, and spectral width. The signal-to-noise ratio and noise level are used to compute equivalent reflectivity (dBZ_e) at each height. The system parameters are given in the last column of Table 4.

TABLE 4. Radar parameters.

	CPRS W band	CPRS Ka band	NOAA S band
Frequency (GHz)	94.92	33.12	2.835
Transmit polarization	V or H	V or H	V
Receiver polarization	V and H	V and H	V
Peak power (kW)	1.5	120	0.38
Average power (W)	15	120	7.6
Antenna	1-m lens	1-m lens	3-m dish with shroud
Two-way 3-dB antenna beamwidth (°)	0.2	0.6	3.2
Range resolution (m)	30 or 75	30 or 75	105 or 495
Noise figure (dB)	13	11	2.6
Minimum detectable reflectivity (dBZ_e) (R = 1 km, 30-s averaging)	−59	−63	−40
Sample volume size relative to W-band sample volume	1	3	107

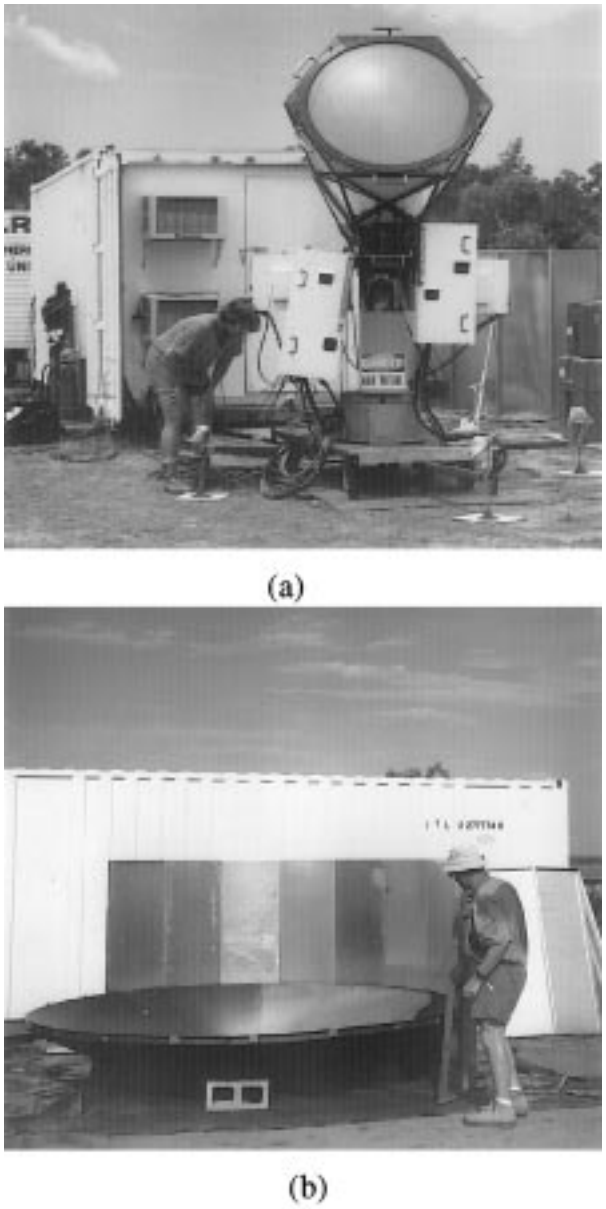

FIG. 1. Cloud radars being installed on Melville Island for MCTEX. (a) UMass 33/95-GHz CPRS and (b) NOAA 2.835-GHz profiler.

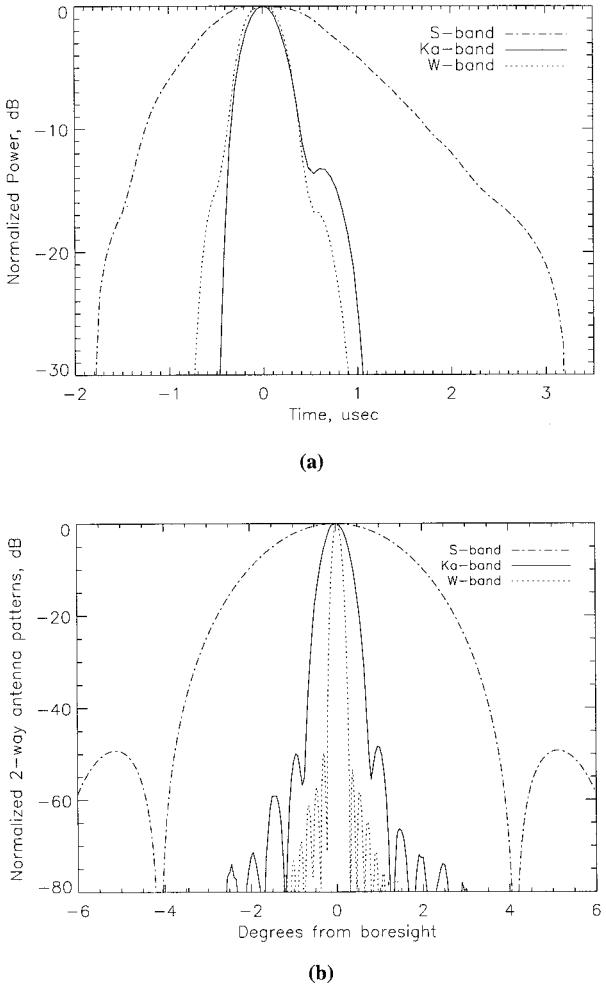

FIG. 2. (a) Range-weighting functions and (b) two-way antenna patterns for CPRS and the NOAA S-band radar.

c. Sample volume matching

Comparison of data is complicated because each radar samples a different cloud volume. Table 4 shows that the −6-dB contour sample volume for the S-band radar is more than two orders of magnitude larger than that of the W-band radar. To reduce the mismatch we degrade the resolution of Ka- and W-band measurements to match those of the S-band system. Our approach is to convolve the Ka- and W-band data in range with the S-band range-weighting function W_r, shown in Fig. 2a and in time (horizontally) with a weighting function, $W_t(t, R)$, which is a function of the S-band antenna pattern. Because the target is not stationary, horizontal cloud motions and radar averaging time must also be factored into the sample volume correction. The term $W_t(t, R)$ is the convolution of a time-averaging function, W_{T_A}, and antenna pattern weights, $W_{\text{ant}}(t, R)$, which are defined below. Here W_{T_A} is the boxcar function

$$W_{T_A}(t_o) = \begin{cases} 1, & -T_A/2 < t_o - t < T_A/2, \\ 0, & \text{otherwise}, \end{cases} \tag{5}$$

and represents temporal averaging of radar returns over T_A seconds about time t_o. The antenna-weighting function depends on the angle with respect to the antenna boresight θ and can be reparameterized as a function of time and range:

$$W_{\text{ant}}(t, R) = W_{\text{ant}}\left\{\sin^{-1}\left[\frac{tV_h(R)}{R}\right]\right\}, \tag{6}$$

where $V_h(R)$ is the horizontal wind speed at height R.

Figure 3 plots $W_t(t, R)$ for $T_A = 30$ s at $R = 2$ km

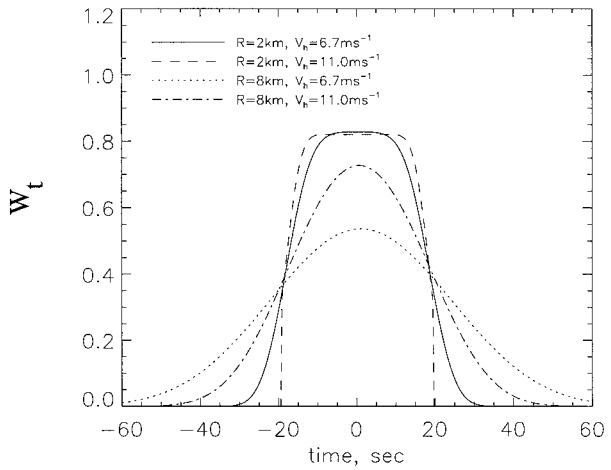

FIG. 3. Examples of time (horizontal) weighting functions for S-band radar illustrating dependence upon horizontal winds. Averaging time, T_A, is 30 s.

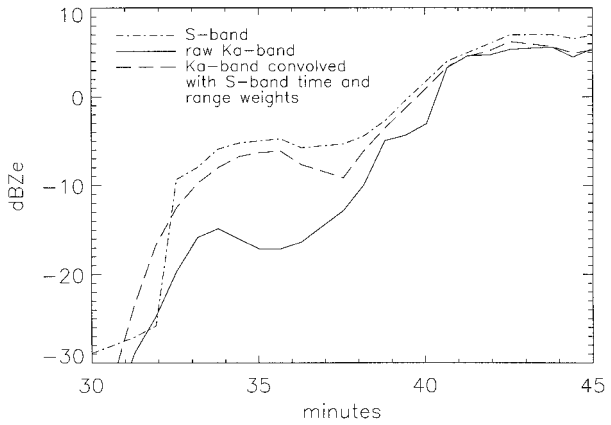

FIG. 4. Results of sample volume matching for cloud edge with a sharp reflectivity gradient.

and $R = 8$ km. If the magnitude of horizontal wind is uniform with height, then W_t becomes wider with height, and the horizontal resolution degrades. The effect is analogous to that for a scanning radar where the effective beam is wider than that of a stationary antenna. However, in this case the radar is fixed and the target is moving across the beam. When the horizontal wind speed increases with height, W_t changes less with height. This situation often occurs, tending to reduce the horizontal resolution dependence on height. Figure 4 illustrates the performance of the volume matching scheme by comparing S- and Ka-band measurements of a sharp reflectivity gradient.

3. Particle size estimation with multifrequency radar

To understand how DWR is affected by density and size distribution shape we evaluate several particle scattering models. First, a comparison of Mie and Rayleigh models for a monodisperse distribution of liquid and frozen spheres of constant density shows the minimum size for which non-Rayleigh scattering is observed at W band (95 GHz). Next, we consider a more realistic ice-cloud model where the particle density decreases with D and the number concentration is modeled by a gamma size distribution. This generalized model describes DWR for both aggregates and spherical approximations of crystals. In the following section this model generates training data for a neural network that combines $\mathrm{DWR}_{\mathrm{Ka,W}}$, $\mathrm{DWR}_{\mathrm{S,W}}$, and $\mathrm{DWR}_{\mathrm{S,Ka}}$ to form estimates of size distribution parameters for measured radar data. Distributions of columns and plates are also modeled to show how ice crystal shape and orientation influence DWR. Scattering for these particles is calculated using the the Discrete Dipole Approximation (DDA). Results show that DWR for planar crystals is highly dependent upon orientation, which agrees with previous investigations. Finally, there is a discussion of polarization effects, which have little influence on the zenith-pointing radar data presented.

a. Non-Rayleigh scattering from spheres

At millimeter wavelengths, differences between measured backscatter and that predicted by the Rayleigh approximation are observed for precipitation and cloud particles (Lhermitte 1988). Figures 5a,b show how W-band scattering departs from the Rayleigh approximation and illustrates how Mie scattering is dependent upon hydrometeor phase and density. Figure 5a plots the ratio of Rayleigh to Mie backscatter at 94.92 GHz for monodisperse distributions of liquid and frozen water spheres with diameters up to 10 mm. Figure 5b shows details of the same curves for diameters less than 1 mm. Rayleigh backscatter efficiency is calculated with $\xi_b = (4\pi^4\lambda^{-4})D^4|K|^2$ and Mie backscatter efficiency with a formulation of the Mie coefficients described by Deirmendjian (1969). Figure 5b shows that the degree of non-Rayleigh scattering for water spheres is somewhat sensitive to temperature. Non-Rayleigh scattering for ice spheres varies little with temperature but is sensitive to density. Variations of $|K|^2$ with temperature are so small that the 0°C backscatter data for ice plotted in Fig. 5 are indistinguishable from the same quantities calculated at −30°C (not shown).

b. Generalized DWR model for aggregates and crystals

Generation of model hydrometeor data is a daunting task given the variety of cloud and precipitation particles found in the atmosphere. However, if we restrict our focus to dry ice particles, simplifications can be made such that a single model represents distributions of both ice crystals and aggregates. The generalized DWR model assumes spherical particles, a variable size–density

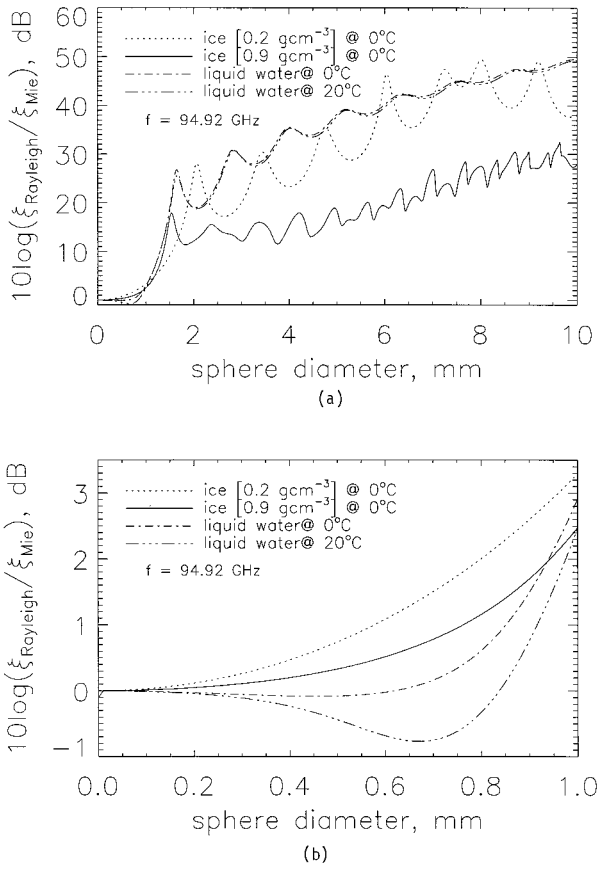

FIG. 5. (a) Ratio of Rayleigh to Mie backscattering efficiencies for liquid water droplets and ice spheres. (b) Detail for small diameters illustrating when Mie scattering occurs.

relationship, and a gamma size distribution described by Ulbrich (1983), which is given by

$$N(D) = N_o D^{\mu} \exp[-(3.67+\mu)D/D_o]. \quad (7)$$

Here, N_o [mm$^{-(\mu+1)}$ m^{-3}] is the peak number concentration, D_o [mm] the median volume diameter, and μ is the dimensionless order of the distribution that determines its shape. The shape is concave upward for $\mu < 1$ and concave downward for $\mu > 1$. The gamma distribution is often used to model cirrus particle distributions (Kosarev and Mazin 1991; Matrosov et al. 1992; Matrosov 1993). Distributions of aggregates or snow tend to follow an exponential size distribution (Sekhon and Srivastava 1970; Thomason et al. 1995), which is also represented by (7) with $\mu = 0$. For the generalized model we apply (7) to distributions of both crystals and aggregates.

As previously mentioned, DWR for spheres is primarily a function of D_o, while reflectivity depends upon D_o, N_o, μ, and $\rho(D)$. The retrieval problem is underconstrained, having three radar measurements and four variables. Therefore, density must be properly modeled in order to retrieve N_o from reflectivity data. Recent publications by Atlas et al. (1995), Brown and Francis (1995), and Thomason et al. (1995) discuss the requirement for improved bulk density parameterization. Density is often treated as a constant, independent of size. However, for aggregates and most crystal habits small particles tend be more dense than larger ones. Most size–density relationships follow the form

$$\rho(D) = \begin{cases} 0.916, & D < (A/0.916)^{B}, \\ AD^{B}, & D > (A/0.916)^{B}, \end{cases} \quad (8)$$

where ρ is in grams per cubic centimeter. The variable A is a positive constant and B is negative, typically close to -1 (Locatelli and Hobbs 1974; Magono and Nakamura 1965; Mitchell et al. 1990).

It can be shown that Z_e is explicitly related to density for Rayleigh scatterers. First, we note that for ρ [g cm^{-3}], $(|K|/\rho)^2 = 0.208$ is nearly constant with ice density (Battan 1973; Atlas et al. 1995) and virtually independent of frequency and temperature for the wavelengths considered. By substituting $\xi_b = (4\pi^4/\lambda^4)D^4|K|^2$, equation (8) and the above constant for $(|K|/\rho)^2$ into (3) we obtain

$$Z_e \approx |K_w|^{-2} N_o 0.208 A^2 \times \int_0^{\infty} D^{6+\mu+2B} \exp[-(3.67 + \mu)D/D_o]\, dD. \quad (9)$$

Note that the above expression is approximate since two residual terms are omitted. These account for the constant density for $0 < D < A/0.916$. However, the error incurred in neglecting these terms in (9) is small. Using a relationship given by Ulbrich (1983), (9) is rewritten in a nonintegral form:

$$Z_e = |K_w(\lambda)|^{-2} N_o 0.208 A^2 \times \left[\frac{\Gamma(7 + \mu + 2B)}{(3.67 + \mu)^{7+\mu+2B}}\right] D_o^{7+\mu+2B}, \quad (10)$$

which explicitly shows the relationship between Z_e, density, and the three gamma distribution parameters. Given that $B \approx -1$, Eq. (10) can be further reduced:

$$Z_e = |K_w(\lambda)|^{-2} N_o 0.208 A^2 \times \left[\frac{\Gamma(5 + \mu)}{(3.67 + \mu)^{5+\mu}}\right] D_o^{5+\mu}. \quad (11)$$

Equation (11) is valid for Rayleigh-scattering particles and can be considered accurate at S band.

Next, we investigate the sensitivity of DWR to density and μ by calculating DWR for the Mitchell et al. (1990) and Brown and Francis (1995) size–density functions using Deirmendjian's formulation of the Mie coefficients (Deirmendjian 1969) and the Weiner density function described in the appendix. Brown's density function for cirrus particles has the following form:

$$\rho(D) = \begin{cases} 0.916, & D < 0.1 \text{ mm}, \\ 0.0706D^{-1.1}, & D > 0.1 \text{ mm}, \end{cases} \quad (12)$$

where ρ is in grams per cubic centimeter and D is in millimeters. For $D < 0.1$ mm density is assumed to be that for solid ice. Snowflake density derived from recent measurements by Mitchell et al. (1990) has the following size dependence:

$$\rho(D) = \begin{cases} 0.916, & D < 0.19 \text{ mm}, \\ 0.17D^{-1}, & D > 0.19 \text{ mm}, \end{cases} \quad (13)$$

where ρ [g cm^{-3}] is density and D [mm] is the maximum particle dimension. These two functions were chosen since they represent vastly different ice particle types.

DWR models plotted in Figs. 6a,b show little difference between the two density functions. The shaded regions represent DWR for a gamma size distribution with $-1 < \mu < +1$. The dashed boundary of each family of curves corresponds to $\mu = -1$ and the solid boundary to $\mu = 1$. DWR for the two density functions do not substantially differ even though absolute reflectivity values for the Mitchell density function are higher than those corresponding to the Brown density function. Figure 6 indicates that $DWR_{Ka,W}$ and $DWR_{S,W}$ become sensitive to particle size distribution shape for D_o greater than approximately 2 mm. $DWR_{S,Ka}$ shows much less sensitivity to size distribution shape, suggesting that $DWR_{S,Ka}$ is better suited to estimate D_o for large snowflakes.

c. DDA models of DWR for crystals

To assess the validity of our generalized scattering model we compare the above results to realistic models of columns and hexagonal plates. These results are calculated using the DDA with details given in the appendix. Previous models of DWR developed for millimeter-wave frequencies present scattering for spheroids (Matrosov 1993) and various realistic ice crystal geometries and orientations common to cirrus clouds (Tang and Aydin 1995; Aydin and Tang 1997). However, these works emphasize the use of frequency pairs with the highest frequency above 95 GHz, and they do not consider aggregated particles.

Figures 7a–e plot DWR for gamma distributions of aggregates and crystals with $D_o < 2$ mm. DWR for aggregates, previously plotted in Fig. 6, are replotted for the smaller size range in Figs. 7a,b for comparison with the DDA results for crystals.

The orientation of plates has a substantial impact on radar backscatter and DWR, and size ambiguities exist for these and other planar crystals because of uncertainties in their orientation. Plates normally lie with the position of their major axes distributed about the horizontal plane (Platt 1978; Hendry et al. 1976), and measurements of the tilt angle distribution suggest a Gaussian shape (Sassen 1987b). The tilt angle is defined as the angle between the major axes of the hexagon and the horizontal plane. Figures 7c,d show DWR for hexagonal plates with a Gaussian distribution of tilt angles

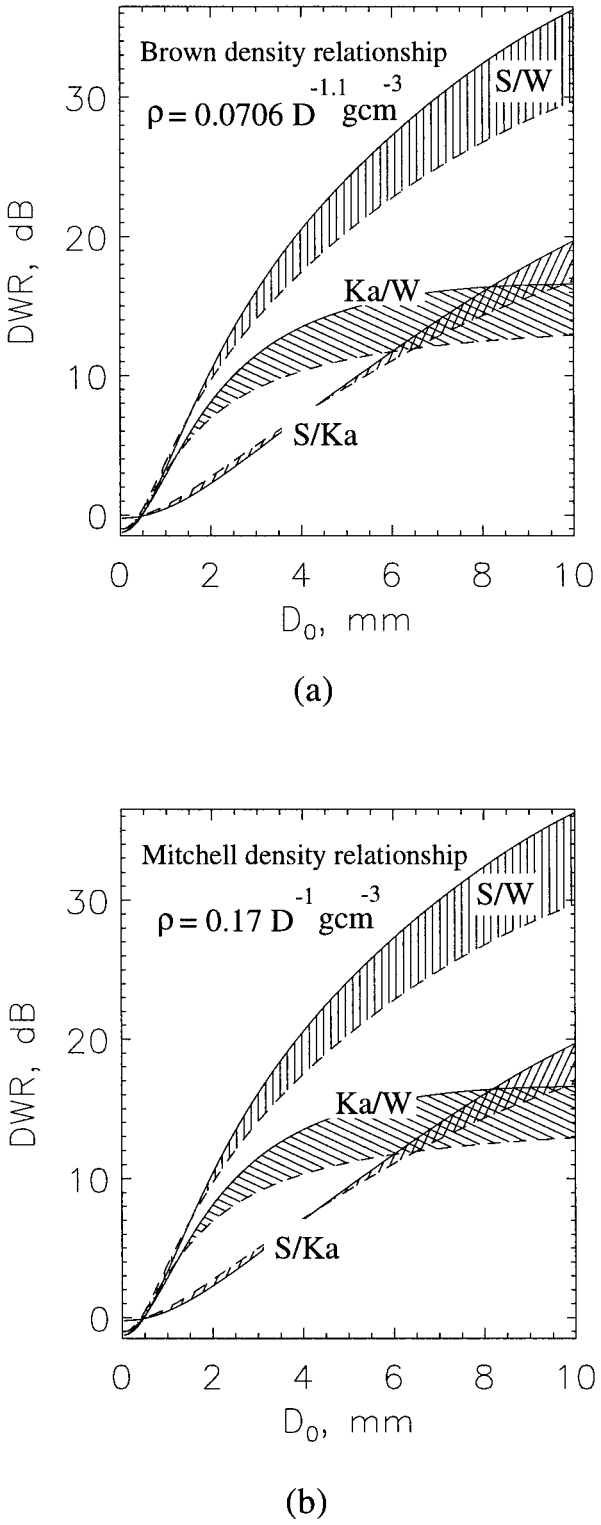

FIG. 6. DWR vs median particle diameter for (a) Brown and (b) Mitchell aggregate density functions. Here, D is in millimeters for the density relationships shown. A general gamma size distribution is assumed with $-1 < \mu < 1$. The dashed boundary corresponds to $\mu = -1$ and the solid boundary corresponds to $\mu = +1$.

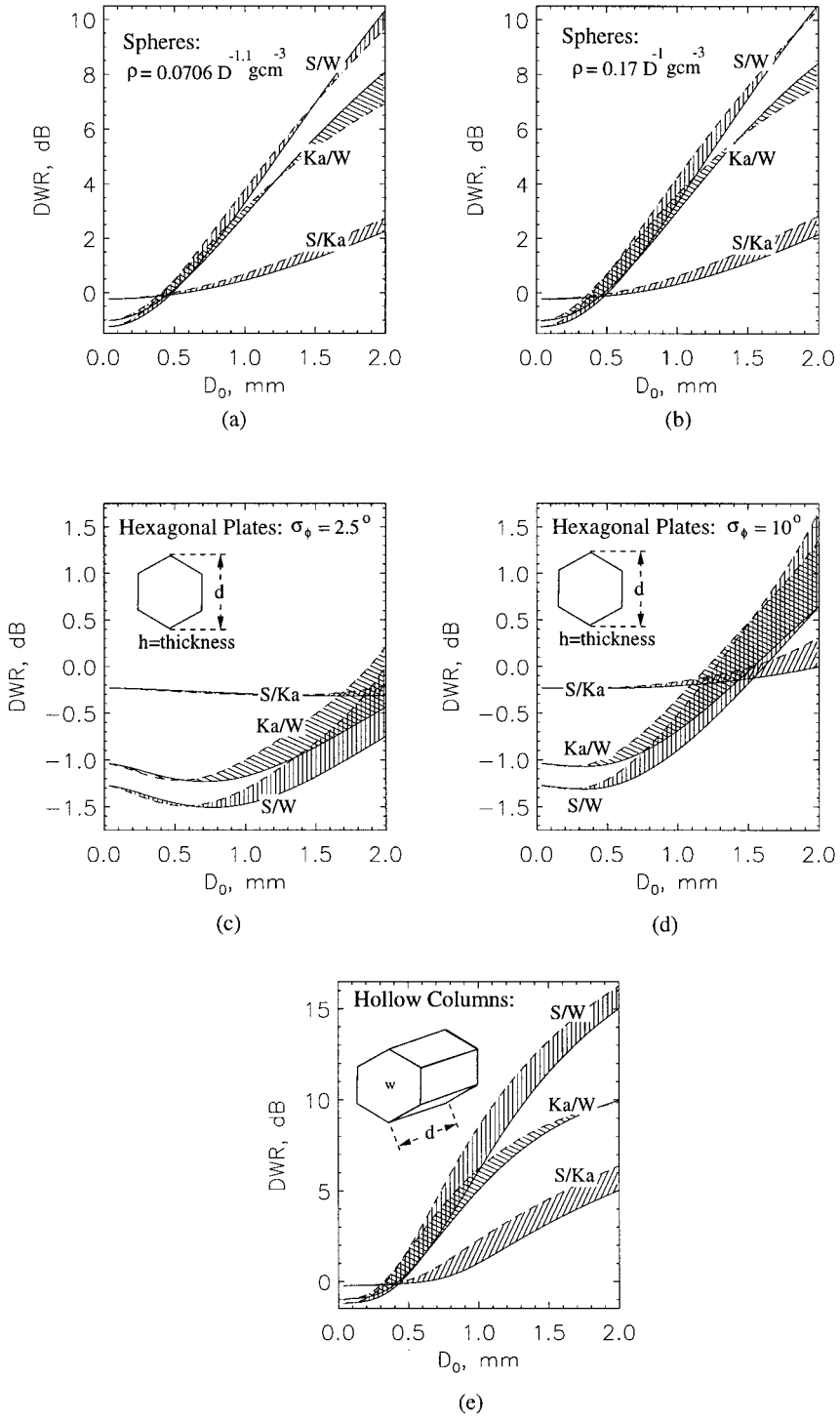

FIG. 7. DWR vs D_o for several aggregate density functions and crystal types. A gamma distribution is assumed with 0 mm $< D_o <$ 2 mm and $-1 < \mu < 1$. Spheres with (a) Brown and (b) Mitchell size–density functions. Hexagonal plates with Gaussian distributions of tilt angles having σ equal to (c) 2.5° and (d) 10°. (e) Hollow columns with long axis randomly distributed in horizontal plane.

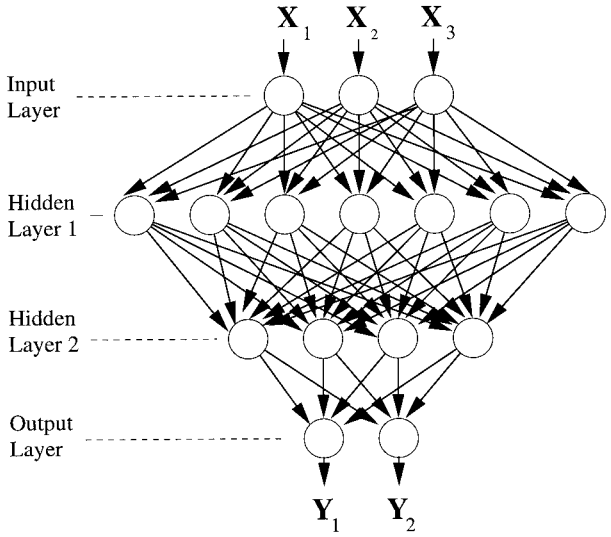

FIG. 8. Geometry of the MLP neural network used to estimate particle size distribution parameters.

having standard deviations of 2.5° and 10°, respectively. These model results agree qualitatively with previous results for DWR calculated using 95 and 220 GHz (Tang and Aydin 1995).

Figure 7e plots DWR for solid columns. Here the columns lie with their major (long) axis parallel to the horizontal plane and the direction of the major axis randomly oriented in the horizontal plane. These results are similar to those in Figs. 7a,b, although DWR for columns appears to be more sensitive to distribution shape than do spheres.

d. Polarization effects

Up to this point there has been no discussion of polarization effects, which can influence Z_e and DWR. The radar cross section of nonsymmetric particles, such as the columns and hexagonal plates described above, depends heavily on the polarization of the incident electromagnetic field and the orientation of the particle relative to the observing radar. However, at zenith incidence these effects are minimal except in cases where crystals are oriented in a preferred direction by electric fields (Metcalf 1995; Galloway et al. 1997).

Previous computational studies of ice crystals at millimeter wavelengths show no difference between horizontal- and vertical-polarized backscatter at zenith incidence. For linear polarizations, differential reflectivity is defined as the ratio of H- to V-polarized reflectivity, $Z_{DR} = 10 \log(Z_H/Z_V)$, expressed in decibels. Models of differential reflectivity for bullet rosettes, columns, and hexagonal plates at 35, 94, and 220 GHz show substantial variation with radar elevation angle (Aydin and Walsh 1996). However, at zenith incidence $Z_{DR} = 0$ for each crystal type.

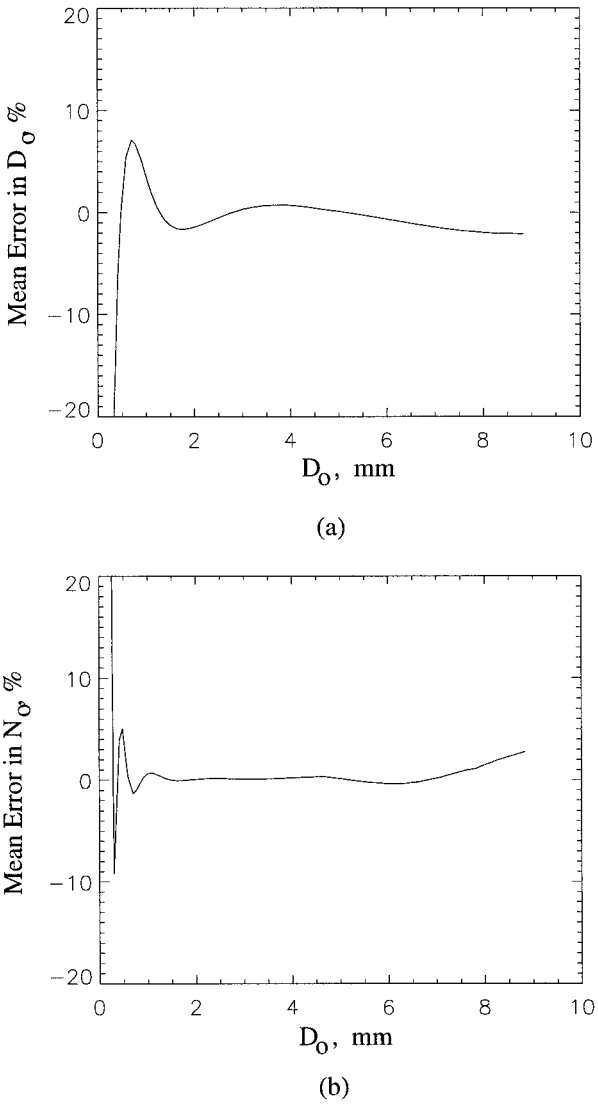

FIG. 9. Mean error in neural network approximation of (a) D_o and (b) N_o for the Brown density function. The curves were created using 10 000 pairs of input/output test vectors, spanning 0.025 mm $\leq D_o \leq$ 9 mm and 100 mm^{-1} m^3 $\leq N_o \leq 5 \times 10^6$ mm^{-1} m^3.

4. Neural network particle size distribution estimator

Although DWR for any single wavelength pair can estimate particle size distribution parameters, quantities derived from a combination of $DWR_{Ka,W}$, $DWR_{S,W}$, and $DWR_{S,Ka}$ can be more precise and noise tolerant. A fundamental question is how to weigh the different DWRs to produce a single estimate of size distribution parameters, especially D_o. In the previous section we noted that $DWR_{Ka,W}$ and $DWR_{S,W}$ show greater sensitivity to change in size than does $DWR_{S,Ka}$ for small D_o. However, $DWR_{S,Ka}$ is less sensitive to μ when D_o is large. Therefore, $DWR_{Ka,W}$ and $DWR_{S,W}$ are best suited to measure small particles and should be weighed more heavily

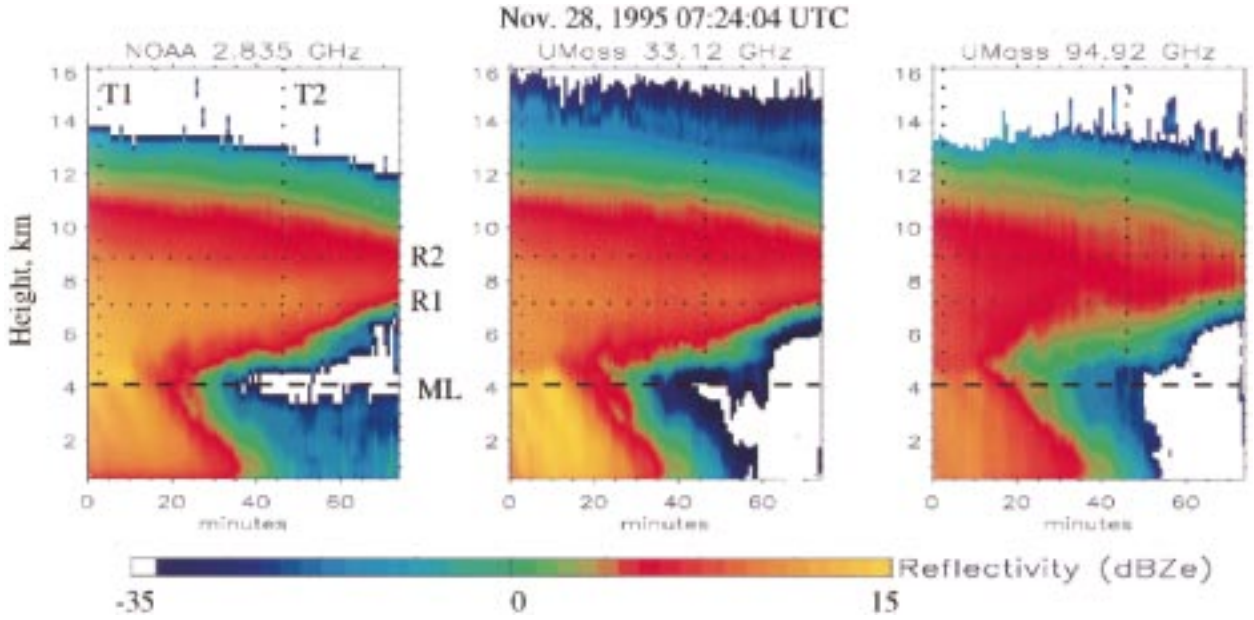

FIG. 10. Radar reflectivity measurements for a stratiform cloud case. Averaging time is 30 s.

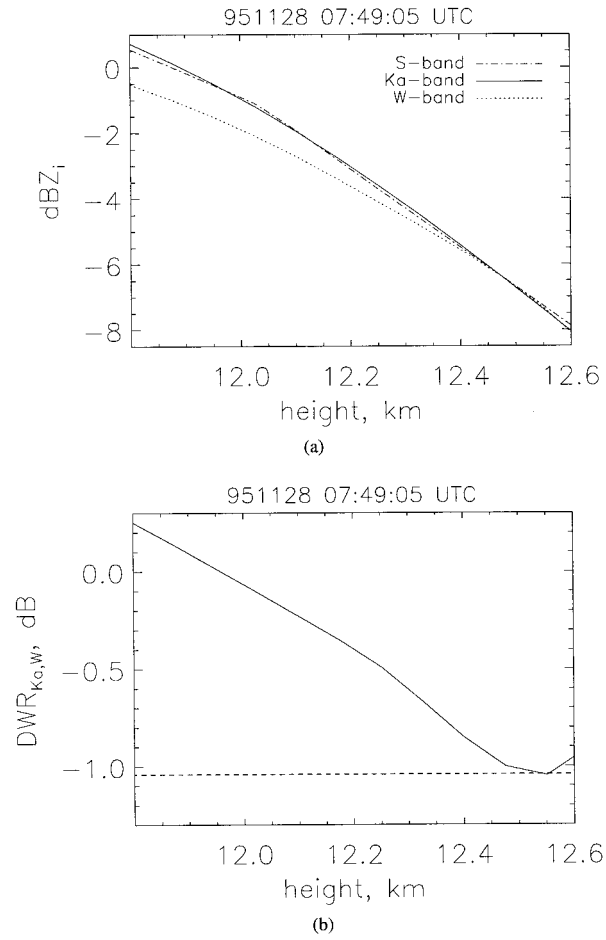

FIG. 11. (a) Ice equivalent reflectivity and (b) $DWR_{Ka,W}$ at stratiform cloud top.

than $DWR_{S,Ka}$ in the smaller particle regime. $DWR_{S,Ka}$ should be weighted more heavily than $DWR_{Ka,W}$ and $DWR_{S,W}$ for distributions of larger particles because $DWR_{S,Ka}$ is less sensitive to μ.

Rather than arbitrarily assign weights to the different DWR values, a neural network was created to estimate median diameter, D_o [mm], and maximum particle concentration, N_o [mm^{-2} m^{-3}], for the first-order gamma size distribution, which is given by (7) with $\mu = 1$. This distribution satisfies $N(0) = 0$ and is a compromise between the exponential distribution describing aggregates and the gamma distribution for cirrus clouds described by Kosarev and Mazin (1991), who indicate that $0 < \mu < 2$. Particle density is assumed to follow Brown's function given by Eq. (12). This assumption affects N_o. Here, D_o is much less sensitive to density, as shown in the previous section.

Neural networks have been used to classify cloud type by Bankert (1994) and Lohmeier et al. (1997), to improve Z–R_r relationships in rain by Xiao and Chandrasekar (1997), and in numerous other engineering and remote sensing applications. For our purposes a neural network approximates the function relating the three radar reflectivity measurements or DWRs to N_o and D_o. Multivariate regression was attempted but found to be numerically unstable and difficult to modify. In contrast, the neural network solution described below is easily modified and more stable over a wide range of input values.

Figure 8 shows the geometry for a fully connected feed-forward multilayered perceptron (MLP) neural network that is used to retrieve particle size distributions. The specific geometry was selected through trial and error such that global errors are minimized,

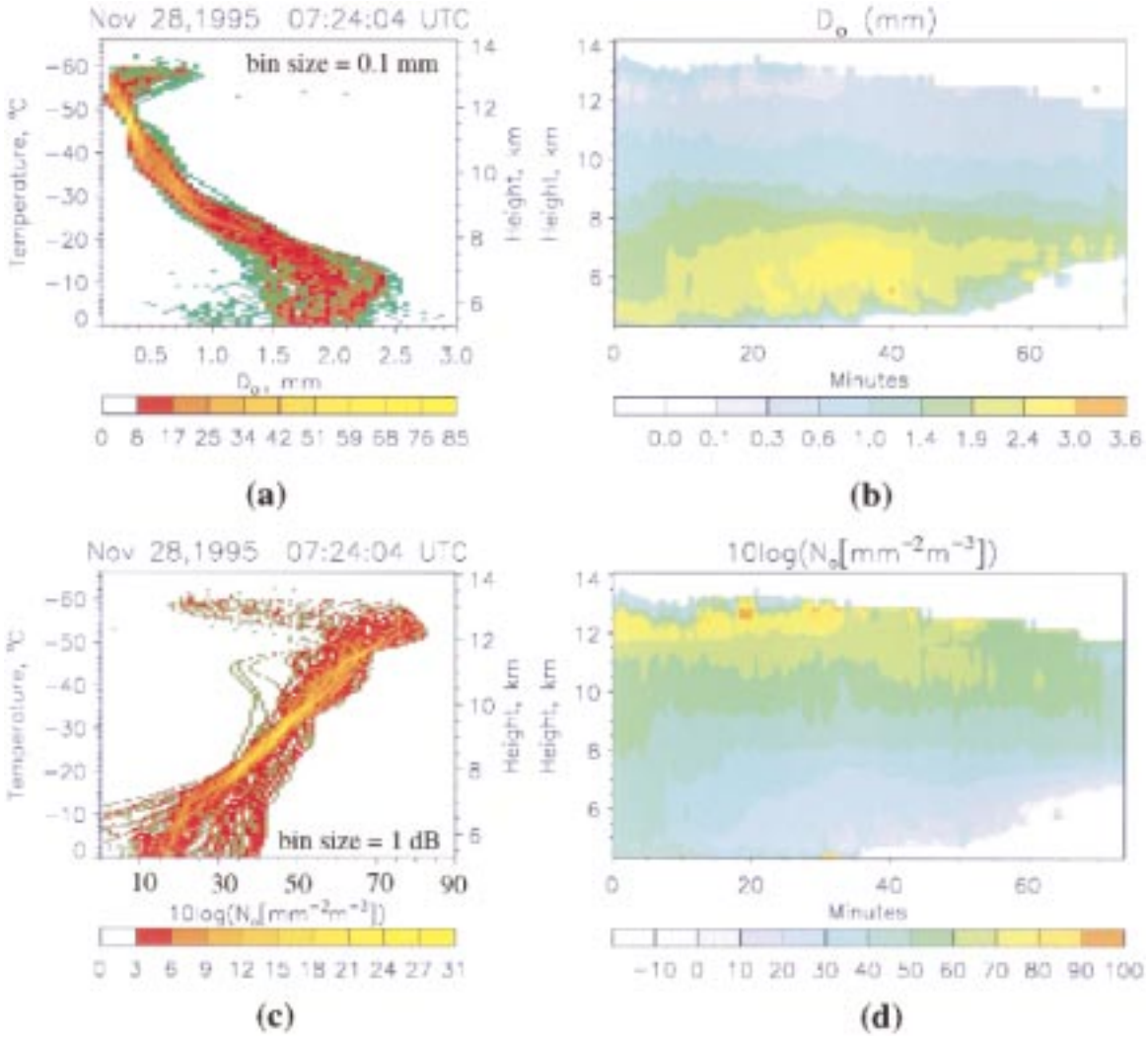

FIG. 12. Neural network outputs for stratiform cloud case using the Brown density function. Data are averaged to 30-s temporal resolution and histograms show number of occurrences for indicated bin sizes. (a) Histogram of D_o, (b) false color map of D_o, (c) histogram of N_o, and (d) false color map of N_o.

and there are no unused nodes. According to Haykin (1994), the universal approximation theorem holds that a three-layer (one hidden) feed-foreword MLP can model a function with arbitrary precision, given that a sufficient number of nodes exists. However, our experience is that a four-layer network (two hidden) train more quickly. Additional practical justification for using two hidden layers is given by Xiao and Chandrasekar (1997).

The neural network shown in Fig. 8 consists of four layers: 1) a layer containing three input nodes, 2) a layer of seven hidden nodes, 3) a second hidden layer of four nodes, and 4) a layer containing two output nodes. Each node contains a nonlinear transfer function, scalar weights for inputs and the output, a bias term, and an activation term that enables the output once the input exceeds a threshold level. The input vector $\overline{\mathbf{X}}$ defined below consists of $\mathrm{DWR}_{\mathrm{S,W}}$ [dB], $\mathrm{DWR}_{\mathrm{Ka,W}}$ [dB], and W-band reflectivity in $\mathrm{dB}Z_e$:

$$\overline{\mathbf{X}} = 0.01[10\log(Z_{e,\mathrm{S}}/Z_{e,\mathrm{W}}),\ 10\log(Z_{e,\mathrm{Ka}}/Z_{e,\mathrm{W}}),\ 10\log(Z_{e,\mathrm{W}})],$$
$$= 0.01[\mathrm{DWR}_{\mathrm{S,W}},\ \mathrm{DWR}_{\mathrm{Ka,W}},\ \mathrm{dB}Z_{e,\mathrm{W}}]. \quad (14)$$

These inputs are equivalent to the three radar reflectivities or three DWR values; that is, $0.01[\mathrm{DWR}_{\mathrm{S,W}}, \mathrm{DWR}_{\mathrm{Ka,W}}, \mathrm{DWR}_{\mathrm{S,Ka}}]$, $0.01[\mathrm{dB}Z_{e,\mathrm{S}}, \mathrm{dB}Z_{e,\mathrm{Ka}}, \mathrm{dB}Z_{e,\mathrm{W}}]$, etc. All contain the same information and may be used instead of (14). Scaled logarithmic values are input to reduce the dynamic range of values that must be modeled by the neural network. The output vector $\overline{\mathbf{Y}}$ is given by

$$\overline{\mathbf{Y}} = 0.01[10\log(N_o),\ D_o]. \quad (15)$$

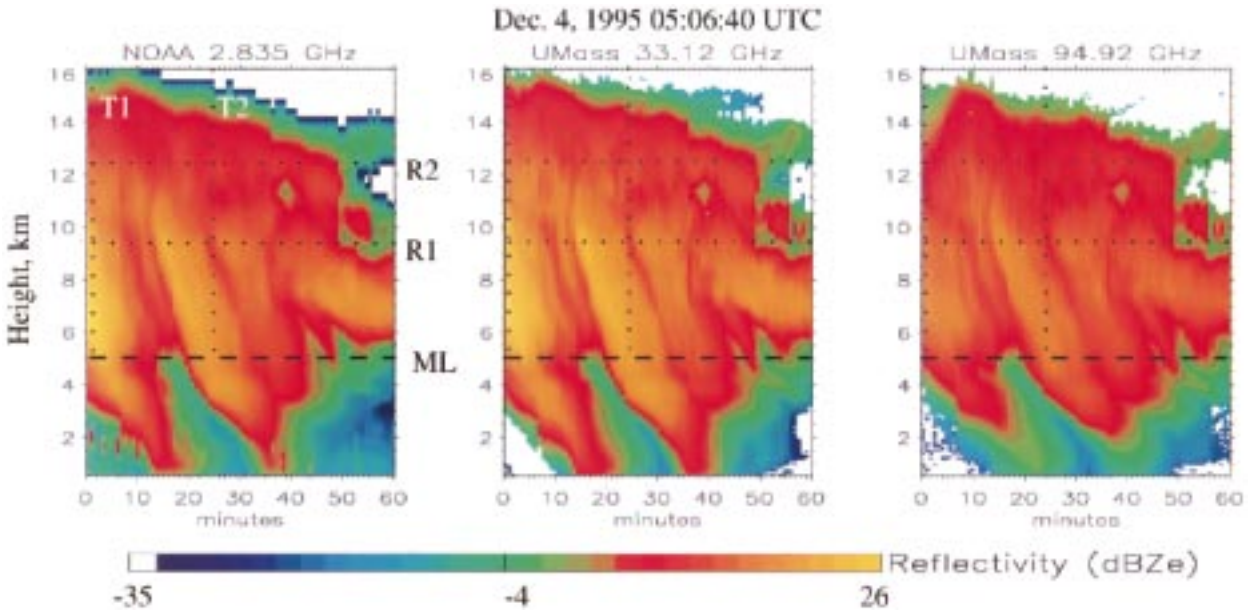

FIG. 13. Radar reflectivity measurements for convective cloud case.

Note that outputs are not coupled to adjacent pixels so our retrieval is performed on a pixel-by-pixel basis.

To generate coefficients for the functions connecting inputs and outputs, the neural network was trained with many input vectors, $\overline{\mathbf{X}}$, and corresponding, known output vectors, $\overline{\mathbf{Y}}$. The bias and weights associated with each node in the network are adjusted according to a training algorithm such that the global difference between the training outputs $\overline{\mathbf{Y}}$ and the neural network outputs $\hat{\mathbf{Y}}$ are minimized. This global difference is determined using the sum of the squared errors (SSE):

$$\text{SSE} = \sum_{i=0}^{N} (\overline{\mathbf{Y}}_i - \hat{\mathbf{Y}}_i)^2. \tag{16}$$

Our neural network was implemented using the Stuttgart Neural Network Simulator version 4.1 (Zell et al. 1995). Standard backpropagation was used to train the neural network with a training dataset that consisted of 12 800 sets of input and output vectors. The network was iterated many times until an acceptable error was achieved with respect to the training data. Here, 120 000 iterations resulted in maximum global error of less than 2%.

To evaluate the performance of the neural network's ability to model its training data, it was tested with 10 000 pairs of input/output vectors that are similar but not identical to the training dataset. Testing with the training dataset can produce inaccurate results. Figure 9a plots the mean error in D_o averaged over all values of N_o, and Fig. 9b plots the mean error of N_o. These figures show a rapid increase in the magnitude of the output errors for D_o less than approximately 0.2 mm. This is an important ramification of the the neural network's inability to build input–output relationships for distributions of small particles.

5. Results

This section presents neural network estimates of particle size distribution parameters and derived quantities using measurements collected during MCTEX, described by Keenan et al. (1995) and Ackerman et al. (1996). MCTEX was conducted on Melville and Bathurst Islands, which lie between 11.3° and 11.9°S, and 130.0° and 130.6°E, approximately 50 km north of Darwin, Australia. Timing of the experiment coincided with the transition from dry to wet season during November and December 1995. During this period, daily convective activity produced numerous thunderstorms and a variety of cloud types were observed by the radars.

Neural network outputs are presented for the following three cloud cases: 1) a precipitating stratiform cloud, 2) a decaying convective cloud producing light drizzle, and 3) the leading edge of a massive cirrus anvil. As described in the previous section the neural network was trained using the Brown density function. While this assumption affects number concentration estimates, it has much less impact on size estimates. Ice mass content (IMC) is also derived from radar reflectivity and the neural network size estimates. Comparison with numerous published Z–IMC relationships shows that the additional size information derived from multifrequency radar data reduces uncertainties in IMC.

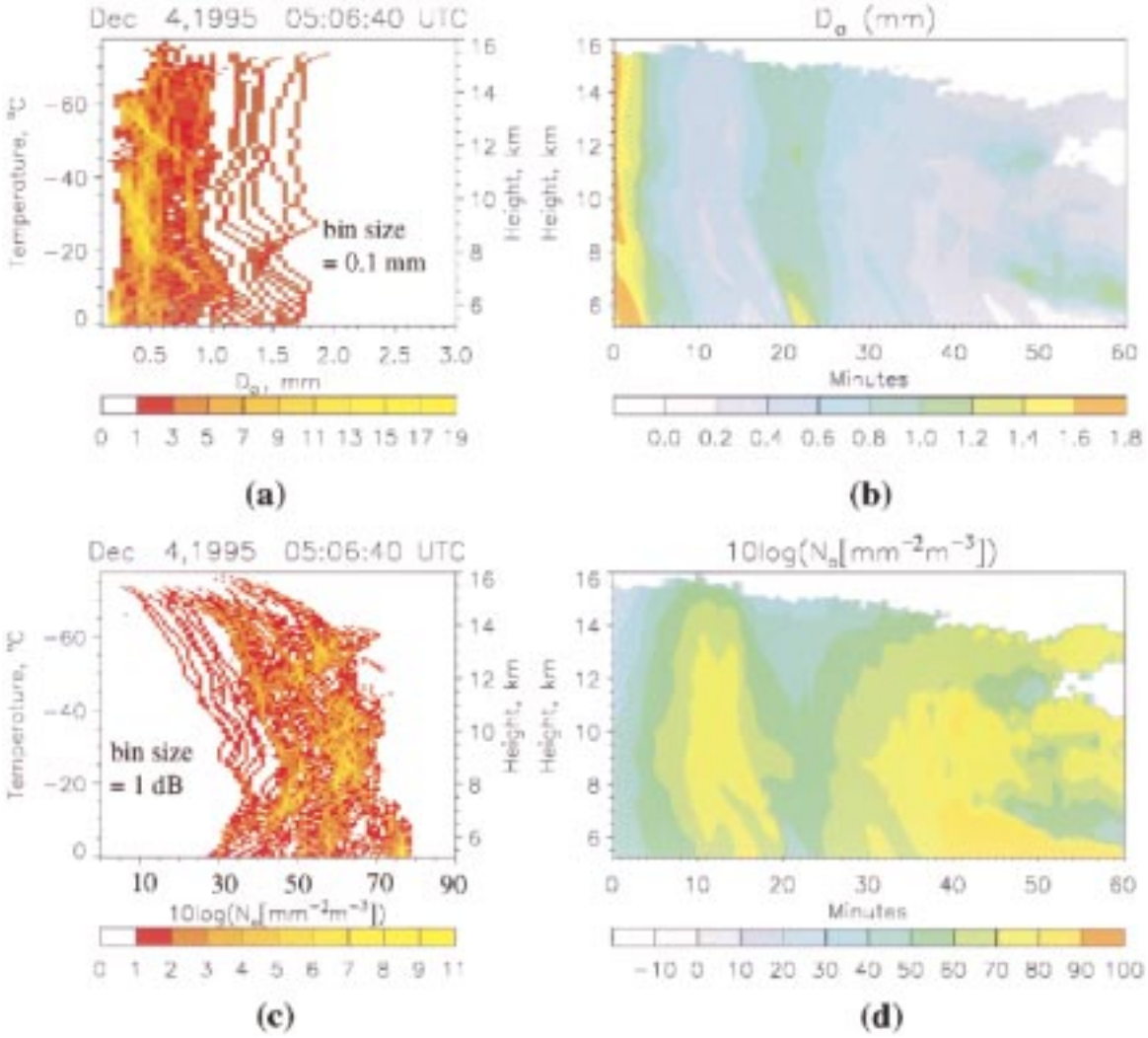

FIG. 14. Same as Fig. 12, except for convective cloud case.

a. Stratiform cloud case

Measurements presented for the stratiform cloud observed on 28 November were collected beginning about 2.5 h after intense convection. Radar Doppler measurements indicate no substantial updrafts, and precipitation ceases approximately halfway through the dataset, shown in Fig. 10. To correct for attenuation effects, cloud-top reflectivities were matched at the different frequencies, taking into account the differences in index of refraction between ice and water given in Table 1. S-band reflectivity values were used as a reference since the S-band signal experiences negligible attenuation.

For ice crystals with small diameters both the Mitchell and Brown size–density functions assume a bulk density for solid ice, and DWR approaches a constant value. The limiting values of DWR for small ice particles shown in Figs. 7a,b are

$$\lim_{D\to 0}(\mathrm{DWR}_{\mathrm{S,Ka}}) = -0.23 \text{ dB}, \tag{17}$$

$$\lim_{D\to 0}(\mathrm{DWR}_{\mathrm{S,W}}) = -1.27 \text{ dB}, \quad \text{and} \tag{18}$$

$$\lim_{D\to 0}(\mathrm{DWR}_{\mathrm{Ka,W}}) = -1.04 \text{ dB}. \tag{19}$$

As previously mentioned, Figs. 7a,b also show that DWR for small D_o is insensitive to the shape of both the size distribution and size–density functions and to particle shape. However, these limits are not approached monotonically for planar crystals. This means that our calibration scheme is insensitive to cloud microphysical parameters provided that the cloud particles are small.

Even though the smallest ice particles are often found near cloud tops, the last range gate showing a signal may not be the best choice for aligning reflectivity data because it may be comprised of volumes sampled above and below the cloud top. In addition, attenuation and

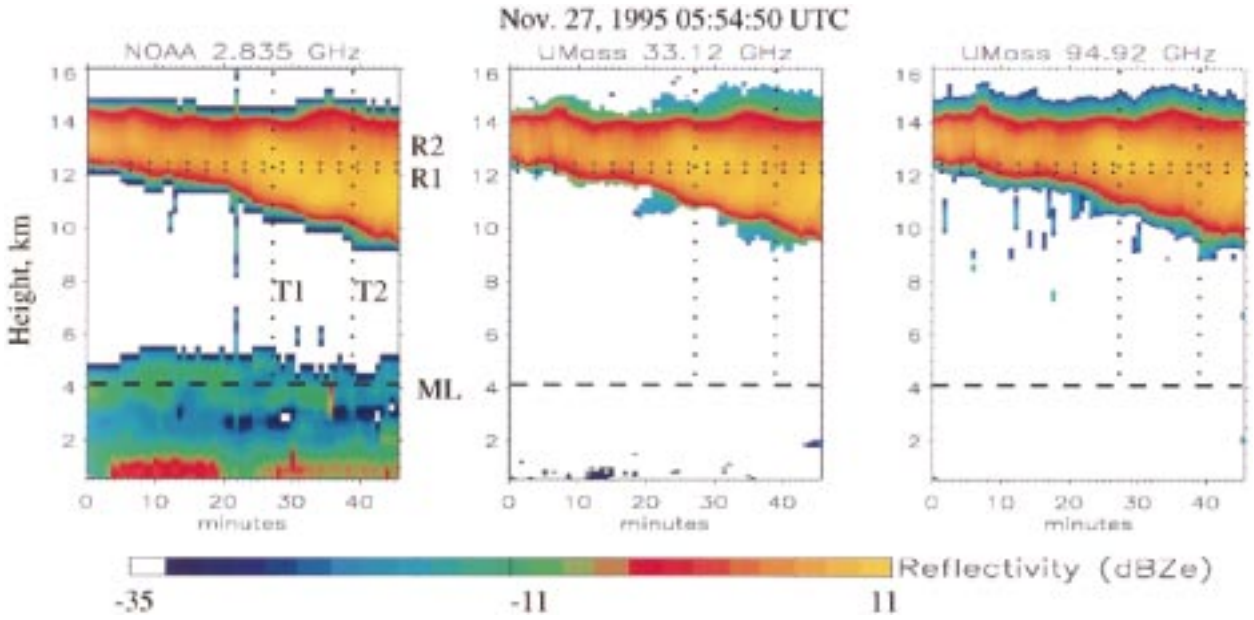

FIG. 15. Radar reflectivity measurements of a cirrus anvil cloud. Note the clear-air return below 6 km at 2.8 GHz, which is not seen by the millimeter-wave radars.

weak cloud reflectivity may prevent one or more of the radar systems from detecting the cloud top. Instead of using the last range gate, a simple algorithm that correlates reflectivity features over small scales is used to determine what range gate close to the cloud top will be used for matching reflectivity values.

The accuracy of the attenuation retrieval must be determined on a case-by-case basis. If all three radars are detecting Rayleigh-sized scatterers at or near cloud top, then DWR calibration is fairly precise, permitting size estimation for $D_o < 0.5$ mm. Figures 11a,b show results of the cloud-top matching for a particular profile. Figure 11a plots ice equivalent reflectivity at the measured cloud top for S, Ka, and W bands. Ice equivalent reflectivity is calculated using data from Table 1 and the following relationship:

$$Z_i = \frac{|K_w|^2}{|K_i|^2} Z_e, \tag{20}$$

as given by Smith (1984). This removes the constant offset between $\mathrm{dB}Z_e$ values created when K_w is assumed instead of K_i so that the overlap in reflectivity is clearly seen. Figure 11b plots $\mathrm{DWR}_{\mathrm{Ka,W}}$. Imperfections in the volume matching scheme limit the accuracy of $\mathrm{DWR}_{\mathrm{S,W}}$ and $\mathrm{DWR}_{\mathrm{S,Ka}}$.

Figures 12a–d show outputs of the neural network estimator for the stratiform cloud presented in Fig. 10. The cloud data used to create these figures were edited such that precipitation and the melting layer are not considered. The first range gate shown corresponds to the freezing level, approximately 4.2 km above ground level, indicated by the dashed line (labeled ML) in Fig. 10. Estimates of median particle diameter, shown as a histogram in Fig. 12a and a time–height plot in Fig. 12b, indicate that D_o monotonically decreases with height. The particle size trend is consistent with previous studies showing aggregate size increasing with temperature (Hobbs et al. 1974). The peak particle concentration shown in Figs. 12c,d increases with height.

b. Convective cloud case

The convective cloud case observed on 4 December is shown in Figs. 13 and 14b–d. It occurred a few minutes after a near miss by a convective cell, but only weak precipitation ($R_r < 1$ mm h^{-1}) fell on the radars. Because the DWR near the cloud-top indicates non-Rayleigh scattering, the cloud-top matching scheme used to remove attenuation for the stratiform case cannot be applied here. Instead, a small correction for attenuation was applied using radar-derived rain rates, assuming Marshall–Palmer drop size distribution (Marshall and Palmer 1948) and combined radiosonde/dual-channel microwave radiometer estimates of water vapor absorption profiles.

Figures 14a,b show that, unlike the stratiform case, there is no particle size trend with height. On smaller timescales, Fig. 14b reveals slanted vertical features centered at approximately 3 and 22 min into the dataset. These correspond to high downward Doppler velocities and become the tops of wind-sheared rain shafts observed below the melting layer. Particle size estimates and radar Doppler data suggest that these features contain large particles falling through a background of smaller, lower terminal velocity particles. Note that

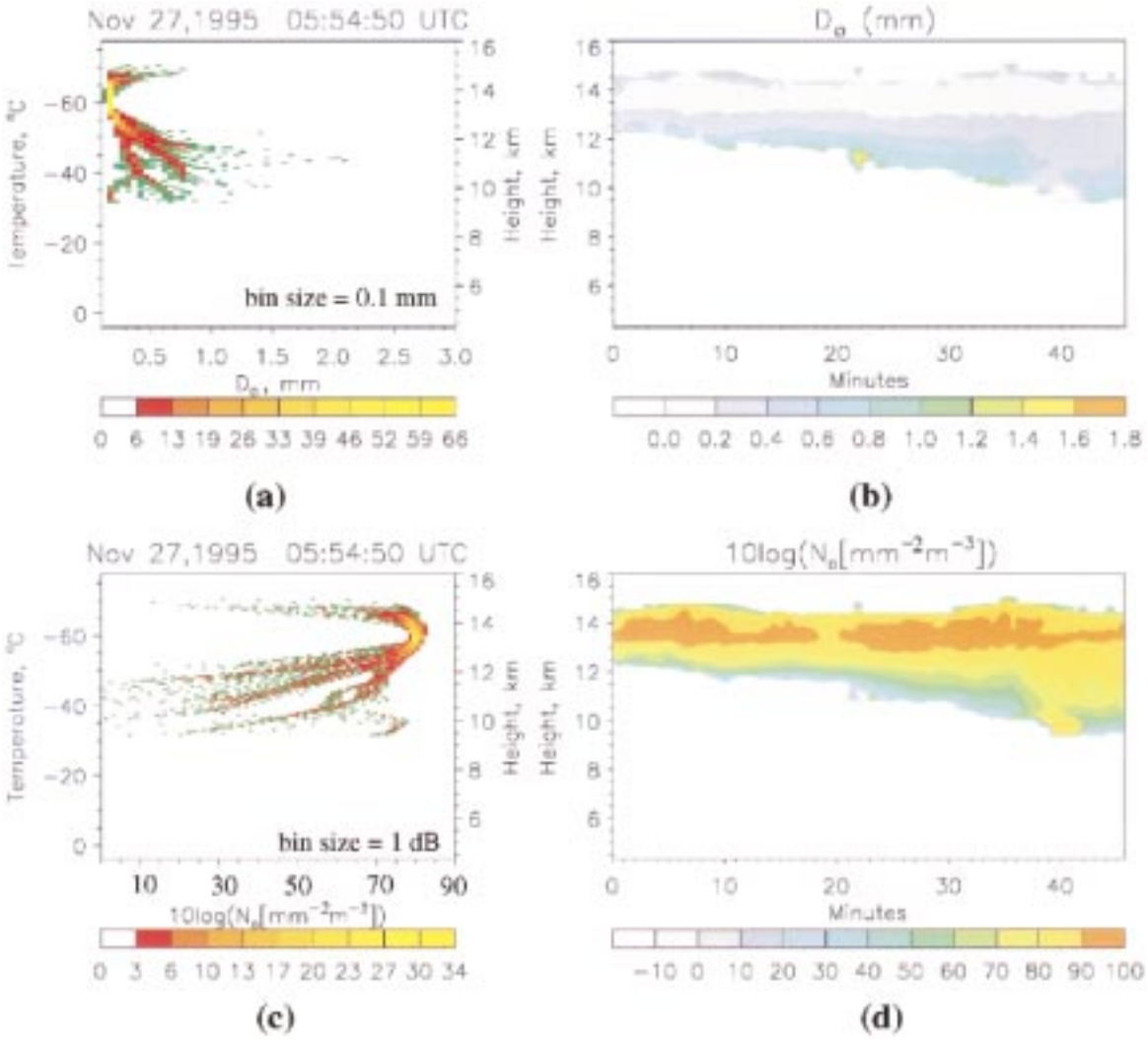

FIG. 16. Same as Figs. 12 and 14, except for cirrus cloud case. As discussed in the text these data are derived using Ka- and W-band data only.

since the neural network considers only radar reflectivity measurements, downdrafts do not influence its particle size estimates as they do when Doppler spectrum measurements are used (Gossard 1994).

c. Cirrus cloud case

The last case analyzed is the leading edge of a large thunderstorm anvil, measured on 27 November, which is shown in Fig. 15. Although Ka-band and W-band radar measurements are well correlated, the cloud is very dynamic and the sample volume matching technique previously described could not adequately adjust for the spatial averaging effects of the S-band radar's wide beamwidth antenna. Fortunately, attenuation in cirrus clouds is small and the S-band measurements are not required to eliminate cloud attenuation. Therefore, the particle size distribution parameters shown in Figs. 16b–d were produced using only CPRS Ka-band and W-band reflectivities. Here we see a trend similar to that for the stratiform case where particle size decreases with height, which is also in agreement with previous in situ measurements of anvils reported by McFarquhar and Heymsfield (1996).

d. Calculation of ice mass content

IMC is an important cloud microphysical parameter determining cloud radiative properties. Various relationships between IMC and radar reflectivity, summarized by Sassen (1987a), have been reported. However, there is large spread in values among these relationships and research to improve them is ongoing (Brown and Francis 1995; Thomason et al. 1995). IMC is defined as

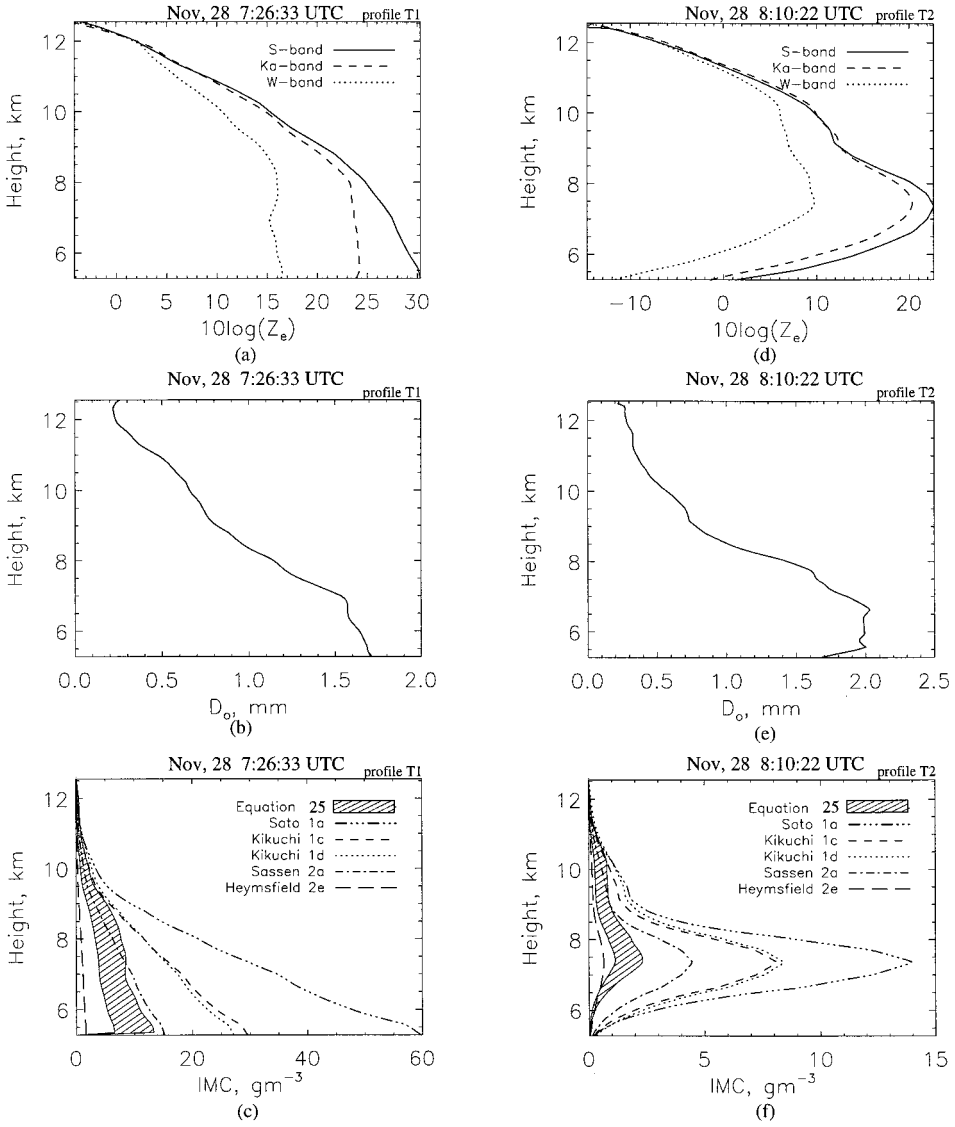

FIG. 17. Vertical profiles of radar measurements and derived quantities for the convective cloud case. (a) Radar reflectivity measurements, (b) neural network estimates of D_o assuming a first-order gamma distribution, and (c) comparison of neural network–derived IMC with published Z_i–IMC relationships (Sassen 1987) corresponding to 0726:33 UTC. Here, (d), (e), and (f) correspond to 0810:22 UTC. The upper bound on hatch regions correspond Brown's density function given by (8), and the lower bound is given by Mitchell's relationship for dry snow.

$$\text{IMC} = 0.001 \int_0^\infty N(D)\rho(D)\left(\frac{4}{3}\right)\pi\left(\frac{D}{2}\right)^3 \text{dD}, \quad (21)$$

where both IMC and ρ are in grams per cubic meter and D is in millimeters.

Equation (21) shows that knowledge of the particle size distribution and density are required to accurately determine IMC. It can be shown that for a gamma size distribution IMC is a function of D_o. Given that $\mu = 1$ and $B = -1$ are reasonable assumptions, then for Rayleigh scatterers the relationship between Z_e and IMC depends only upon A and D_o. Here, D_o is obtained from DWR measurements.

Substituting (7) into (21) results in the following relationship, which gives the dependence of IMC on density and the three parameters of the gamma size distribution:

$$\text{IMC} = 10^{-3} N_o A \left(\frac{\pi}{6}\right)\left[\left(\frac{\Gamma(4+\mu+B)}{(3.67+\mu)^{4+\mu+B}}\right) D_o^{(4+\mu+B)}\right]. \quad (22)$$

For Rayleigh scattering particles, IMC is expressed as

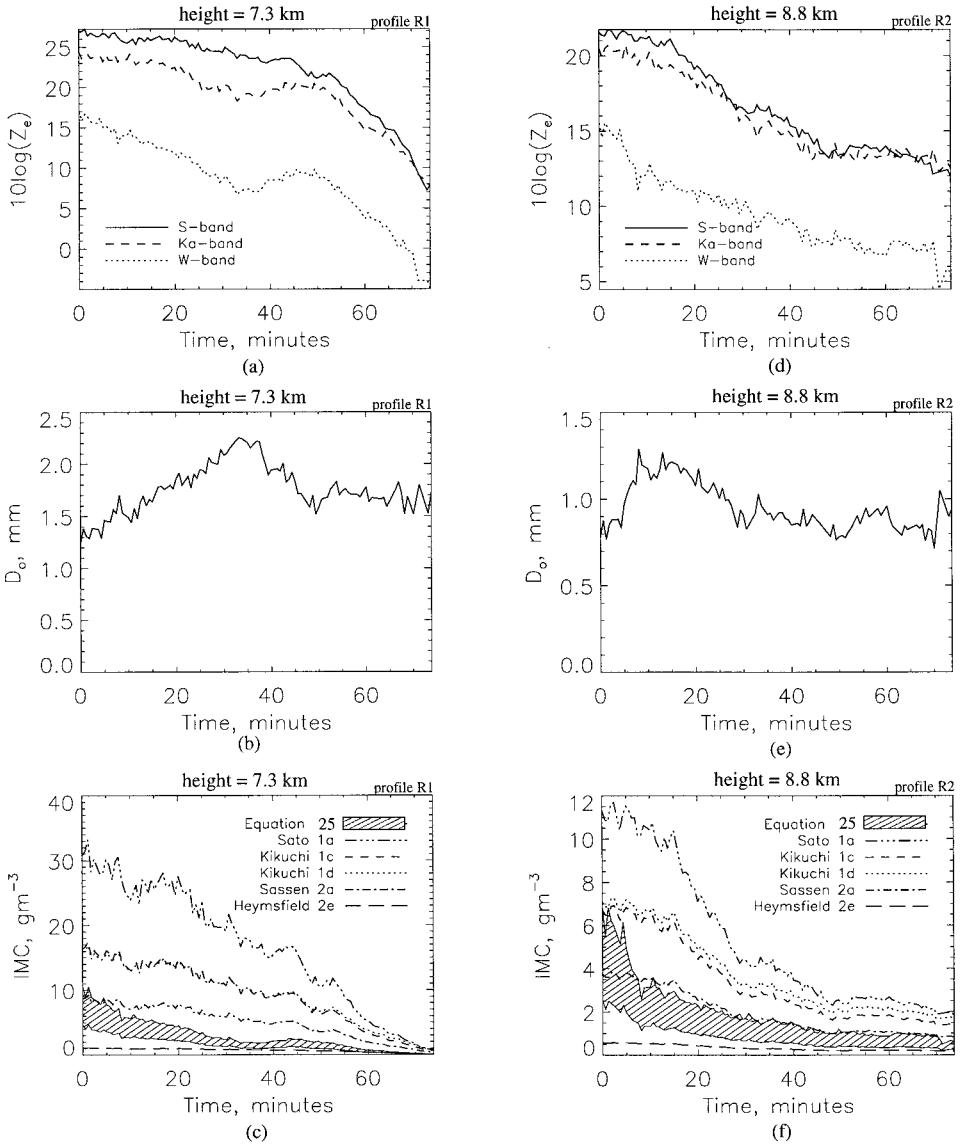

FIG. 18. Profiles of radar reflectivity and derived IMC vs time for the 28 Nov stratiform cloud case. (a) Radar reflectivity measurements, (b) neural network estimates of D_o assuming a first-order gamma distribution, and (c) comparison of neural network–derived IMC with published Z_i–IMC relationships (Sassen 1987) at a height of 7.3 km. Here, (d), (e), and (f) correspond to height of 8.8 km.

a function of radar reflectivity and D_o by combining (10) and (22):

$$\text{IMC} = 10^{-3}Z_e\left(\frac{\pi}{6}\right)\left(\frac{|K_w|^2}{0.208A}\right) \times \left[\left(\frac{\Gamma(4+\mu+B)}{\Gamma(7+\mu+2B)}\right)(3.67+\mu)^{3+B}\right]D_o^{-(3+B)}. \quad (23)$$

The bracketed quantity depends upon μ and B. However, if $B = -1$, then the bracketed quantity varies less than 15% for $-1 < \mu < 3$ and less than 6% for $0 < \mu < 3$. Thus, IMC is fairly insensitive to μ. For $\mu = 1$ and $B = -1$ the bracketed term is 0.485 and (23) reduces to

$$\text{IMC} = 10^{-3}Z_e\left(\frac{\pi}{6}\right)\left(\frac{0.485|K_w|^2}{0.208}\right)A^{-1}D_o^{-2}, \quad (24)$$

or as a function of ice equivalent reflectivity,

$$\text{IMC} = 10^{-3}Z_i\left(\frac{\pi}{6}\right)\left(\frac{0.485|K_i|^2}{0.208}\right)A^{-1}D_o^{-2}. \quad (25)$$

These relationships show that IMC depends linearly upon A, which must be assumed. While this uncertainty in A affects IMC, the variation in IMC is less than the spread

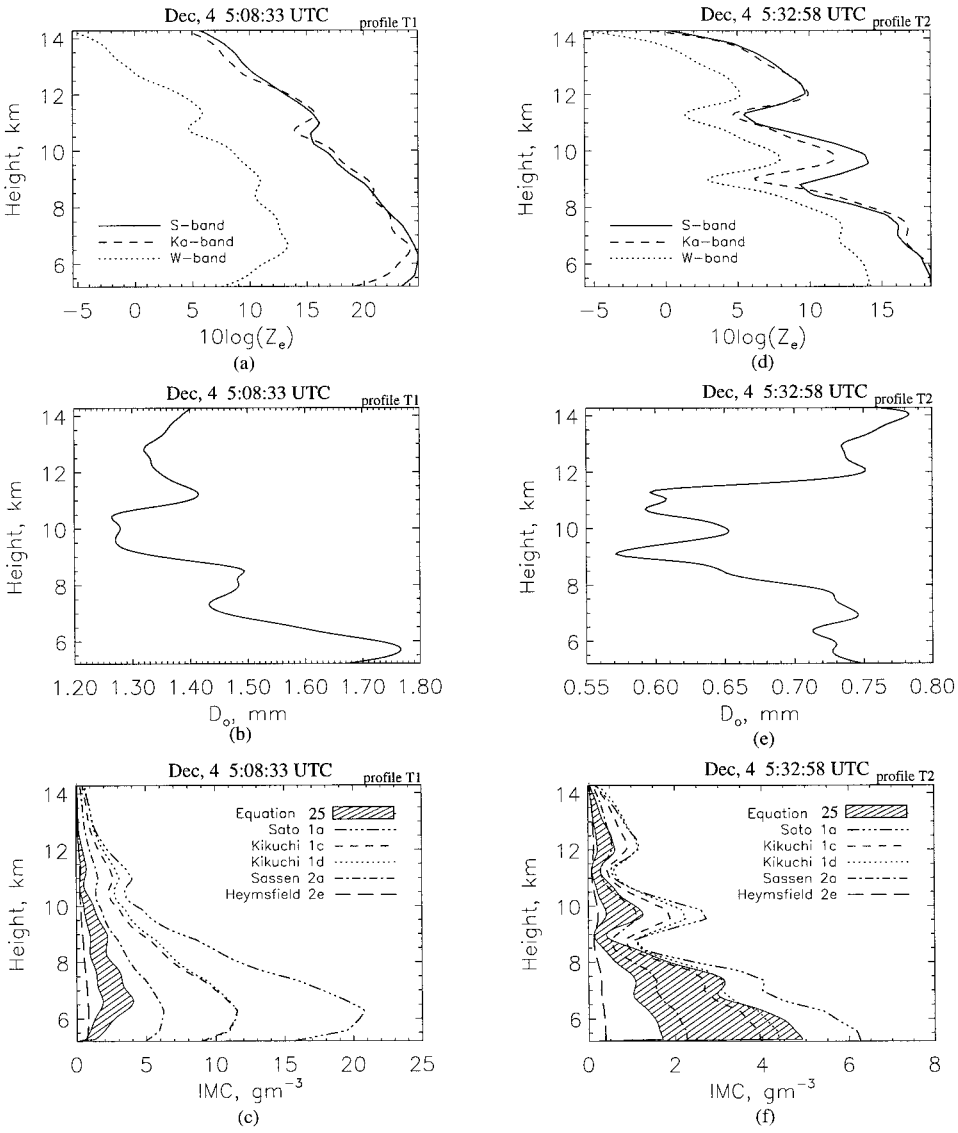

FIG. 19. Same as Fig. 17, except for 4 Dec convective cloud case. Here, (a), (b), and (c) correspond to 0508:33 UTC and (d), (e), and (f) correspond to 0532:58 UTC.

among previous Z_i–IMC relationships for clouds with no corresponding in situ data. Below, profiles of IMC are presented for a realistic range of A coefficients and compared to the Z_i–IMC relationships listed in Table 5.

Figures 17–22 show horizontal and vertical profiles of radar reflectivity, D_o, and IMC for the cloud cases analyzed. Here, IMC calculated using Eq. (25) is compared to values calculated using the Z_i–IMC relationships summarized in Table 5. The hatched region of the IMC plots is bounded by the Brown ($A = 0.0706$, upper bound) and Mitchell ($A = 0.17$, lower bound) density functions and represents the spread of values anticipated for particles ranging from cirrus particles to snowflakes.

Figures 17 and 18 plot profiles corresponding to the dotted lines in the reflectivity image for the stratiform cloud case shown in Fig. 10. The profiles show how IMC calculated with Eq. (25) react to variations in both Z and D_o. For a given value of Z, IMC increases with decreasing D_o. The Z_i–IMC relationships are only affected by Z.

Similarly, the convective case is shown in Figs. 19 and 20. Figure 20 shows interesting discrepancies between Eq. (25) and the Z_i–IMC relationships in the precipitating features seen in Fig. 13 where DWR indicates large particles.

Profiles for the cirrus case plotted in Figs. 21 and 22 show that IMC estimates are degraded for D_o less than approximately 0.2 mm. This is not surprising since $D_o = 0.2$ mm is the minimum size for which DWR, cal-

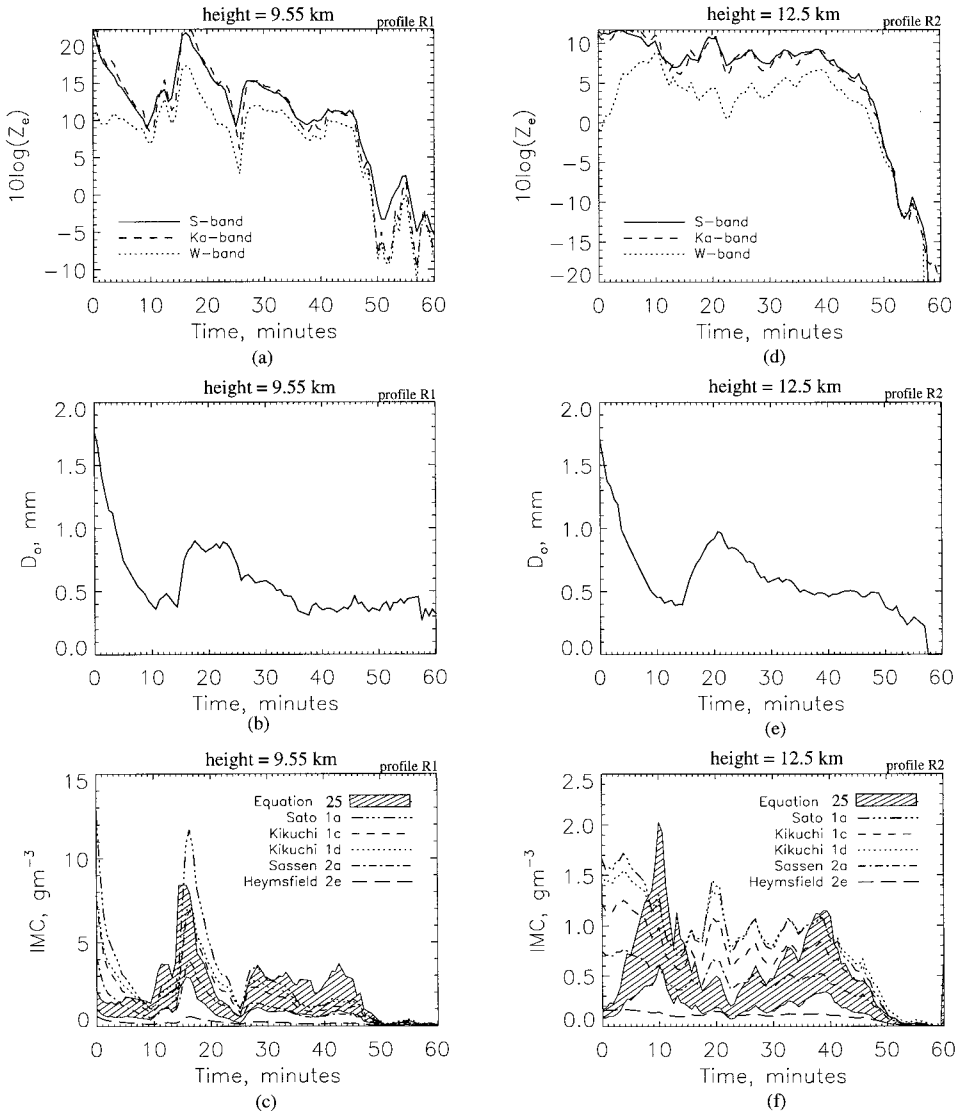

FIG. 20. Same as Fig. 18, except for 4 Dec convective cloud case. Here, (a), (b), and (c) correspond to a height of 9.55 km and (d), (e), and (f) correspond to height of 12.5 km.

culated with the radar wavelengths available, is sensitive to size.

6. Conclusions

Cloud reflectivity measurements collected by multiwavelength radars operating at one or more millimeter wavelengths can estimate median particle size, and other particle size distribution characteristics in clouds composed of dry ice particles for median diameters larger than approximately 0.2 mm. In contrast to techniques requiring lidar or IR radiometer measurements (Matrosov et al. 1992; Intrieri et al. 1993), the multiwavelength radar technique described is substantially less affected by atmospheric attenuation and works for clouds having large optical depths. However, combined lidar–radar and IR–radar techniques are superior to multiwavelength radar for measuring distributions of particles with $D_o <$ 0.2 mm.

For measurements at two radar wavelengths, particle size information is contained in the DWR, which is the ratio of equivalent radar reflectivity measured at the longer wavelength to that at the shorter wavelength. DWR is typically positive although limiting values for small diameters are slightly negative due to the frequency dependent dielectric constant for water used to calculate DWR. Selection of the upper frequency is a trade-off between minimum detectable size and cloud extinction, while the lower frequency sets the maximum size that is detected and is a compromise between attenuation and system portability. Scattering models show that the range of dry particle diameters that can

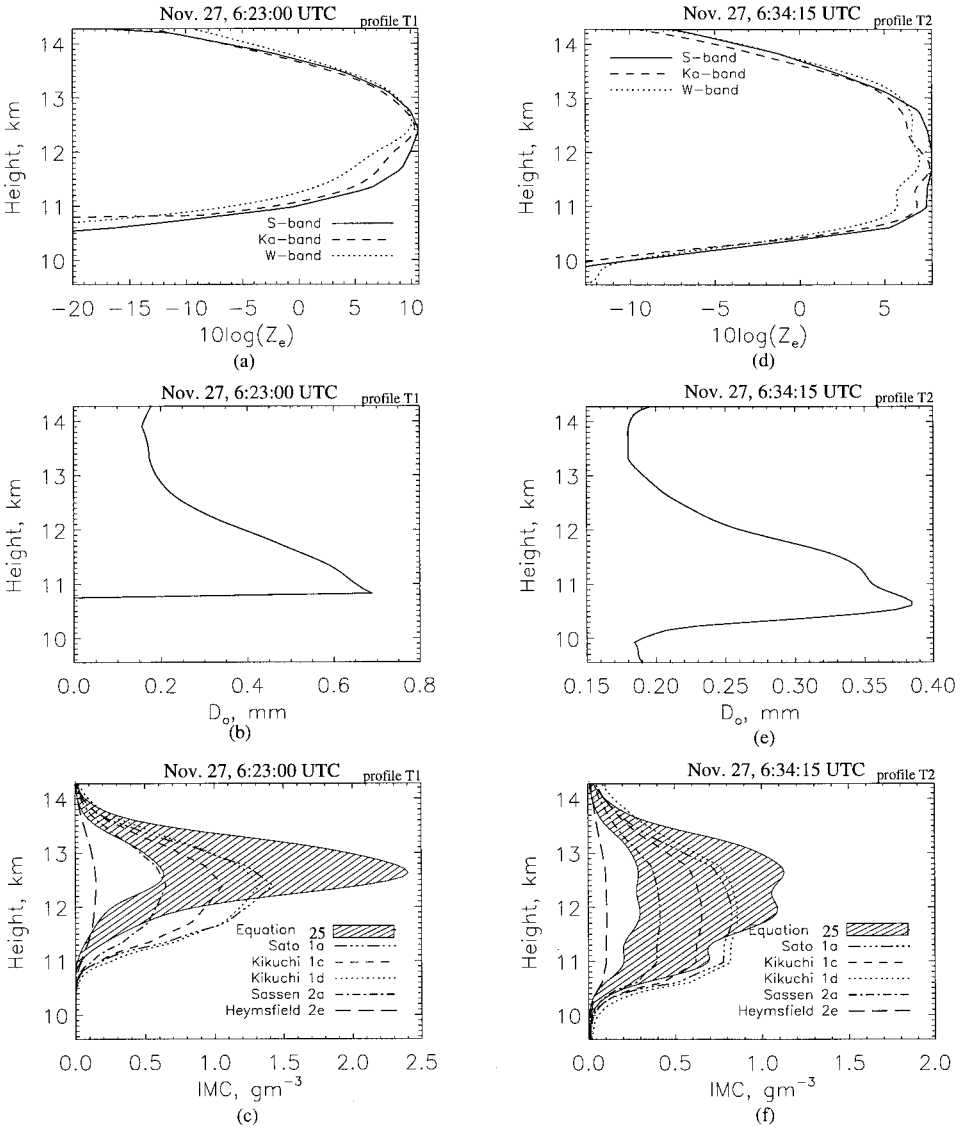

FIG. 21. Same as Figs. 17 and 19, except for 27 Nov cirrus anvil. Here, (a), (b), and (c) correspond to 0623:00 UTC and (d), (e), and (f) correspond to 0634:15 UTC.

be unambiguously estimated using the Ka-band–W-band frequency pair is approximately 0.2–5 mm, while the S-band–W-band pair has the same minimum size limitation but can be used to retrieve much larger particle diameters. The S-band signal also experiences negligible attenuation. There are, however, trade-offs between spatial resolution and system portability for the lower frequency. For instance, the S-band radar requires a substantially larger antenna to match the spatial resolution of the CPRS Ka-band subsystem. Additionally, while measurements of horizontal winds can be used to correct for sample volume mismatches when a wide-beam antenna is employed, the correction does not work well for highly dynamic clouds, such as the cirrus anvil measurements presented.

When measurements are available for more than two radar wavelengths, neural networks are a practical means for weighting the measurements and producing a single estimate of particle size distribution parameters. Using W-band (95 GHz), Ka-band (33 GHz), and S-band (2.8 GHz) radar reflectivity measurements collected during MCTEX, median particle size D_o and peak number concentration N_o are estimated, assuming a first-order gamma distribution for three distinct cloud cases: 1) a precipitating stratiform cloud, 2) a convective cloud, and 3) a cirrus anvil. While histograms of D_o show a characteristic decrease with height in the stratiform cloud and cirrus anvil, no such trend is seen in convective cloud where large particles are detected at all altitudes.

Estimates of IMC are also calculated from the neural network–derived size distributions and compared to Z_i–

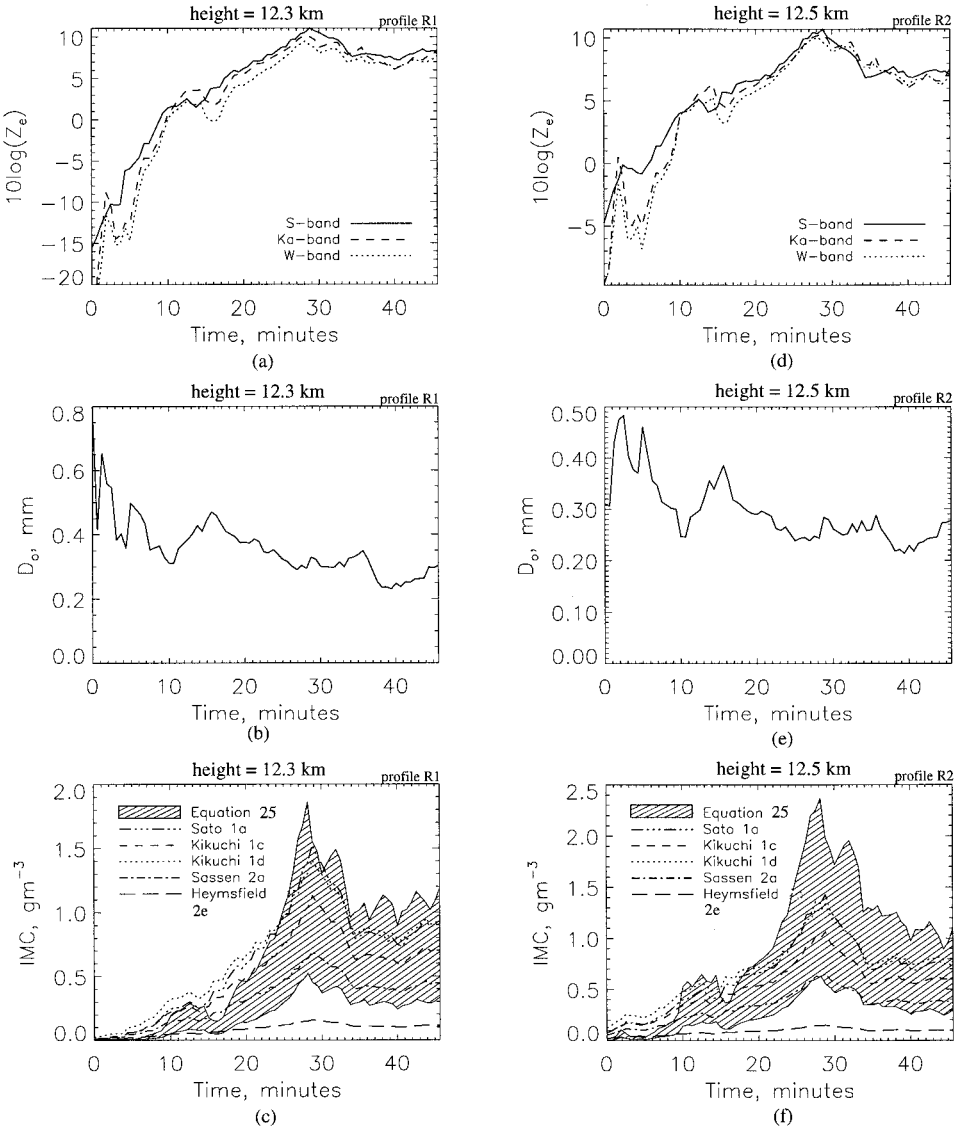

FIG. 22. Same as Figs. 18 and 20 except for 27 Nov cirrus anvil. Here, (a), (b) and (c) correspond to a height of 12.3 km and (d), (e), and (f) correspond to height of 12.5 km.

IMC relationships for various cloud types. The Z_i–IMC relationships listed in Table 5 are statistical in nature and therefore applicable only to specific cloud types, whereas IMC estimates calculated using radar-derived D_o and Eq. (25) do not depend upon cloud type and react to the microphysics of the clouds observed.

TABLE 5. Z_i–IMC relationships described in (Sassen 1987). IMC is in g m^3 and Z_i is in mm^6 m^{-3}.

	Relationship	Cloud type
Sato 1b	IMC = $0.042Z_i^{0.9}$	Deep ice cloud
Kikuchi 1c	IMC = $0.051Z_i^{0.736}$	Deep ice cloud
Kikuchi 1d	IMC = $0.085Z_i^{0.667}$	Deep ice cloud
Sassen 2a	IMC = $0.037Z_i^{0.696}$	Generalized ice cloud
Heymsfield 2e	IMC = $0.017Z_i^{0.529}$	Anvil cloud

Acknowledgments. The radar measurements and data analysis performed by the University of Massachusetts—Amherst were supported by the Department of Energy Atmospheric Radiation Measurement (ARM) program under Grant 352095-AQ5 and Grant DEFG02-90ER61060, respectively. The NOAA Aeronomy Laboratory S-band work was supported in part by the National Science Foundation under Grant ATM-9214800 and by the Department of Energy as part of the ARM program. Special thanks to Dr. Thomas Ackerman of The Pennsylvania State University (PSU) for introducing the University of Massachusetts to MCTEX, to Jay Eshbaugh, Eric Knapp, Lihua Li, Michael Petronino, and Brian Roberts for preparing the sea container and radar hardware, and to Eugene Clothiaux (PSU), Paul Johnston (NOAA), and personnel from the Australian

TABLE A1. Density and dimensional relationships for several particle geometries corresponding to the DWR models in Fig. 7.

Particle geometry	Dimensional relationship	Size–density relationship
Sphere	—	$\rho = 0.0706D^{-1.1}$ g cm^{-3}, D [mm] (Brown and Francis 1995)
Sphere	—	$\rho = 0.17D^{-1}$ g cm^{-3}, D [mm] (Mitchell et al. 1990)
Hexagonal plate	$h = 2.01D^{0.449}$ μm, D [μm] (Auer and Veal 1970)	$\rho = 0.9$ g cm^{-3} (Heymsfield 1972)
Hollow column	$D < 200$ μm: $w = 11.3D^{0.414}$ μm, D [μm]	$\rho = 0.65D^{-0.0915}$ g cm^{-3}, D [μm] (Heymsfield 1972)
	$D < 200$ μm: $w = 0.866D$, μm, D [μm] (Auer and Veal 1970)	

Bureau of Meteorology Research Centre (BMRC) for helping to maintain the CPRS and the NOAA radar on Melville Island.

APPENDIX

Scattering Models for Ice Crystals and Aggregates

a. Index of refraction

The index of refraction, n, for dry ice particles is related to bulk density using Wiener's theorem (Oguchi 1983):

$$\frac{(n^2 - 1)}{(n^2 + 2)} = f_a\frac{(n_a^2 - 1)}{(n_a^2 + 2)} + f_i\frac{(n_i^2 - 1)}{(n_i^2 + 2)}, \quad \text{(A1)}$$

where n_i is the index of refraction for solid ice and n_a is the index of refraction for air. Here, n_i is obtained using data from Ray (1972) and n_a is assumed to have a constant value of unity. Additionally, f_i and f_a are the dimensionless volume fractions of ice and air, respectively, which are subject to the constraints $f_i + f_a = 1$ and $\rho_i f_i + \rho_a f_a = \rho$. Here, ρ_i is the density of solid ice ($\rho_i = 0.916$ g cm^{-3}), ρ_a is the density of air, and ρ is particle bulk density. Combining these constraints the volume fraction of ice is obtained:

$$f_i = \frac{\rho - \rho_a}{\rho_i - \rho_a}. \quad \text{(A2)}$$

Assuming that $\rho_a \ll \rho$ and $\rho_a \ll \rho_i$ this can be further -reduced to

$$f_i = \frac{\rho}{\rho_i}, \quad \text{(A3)}$$

which is accurate except for very low density particles. By substituting (A3) into (A1), the following expression for the index of refraction for dry particles is obtained:

$$n = \frac{2 + n_i^2 + 2f_i(n_i^2 - 1)}{2 + n_i^2 + f_i(-n_i^2 + 1)}. \quad \text{(A4)}$$

b. Backscatter computations for ice crystals

Numerical modeling techniques can accurately determine backscatter for irregularly shaped hydrometeors with maximum dimensions larger than approximately $\lambda/10$, which is typically the maximum size for which the Rayleigh approximation is applied. Bohren and Singham (1991) reviews various methods for calculating radar backscatter and discusses inadequacies of classic approaches such as Rayleigh and Rayleigh–Gans theory. On the other hand, the feasibility of numerical techniques for short radar wavelengths, including Ka band and W band, has been demonstrated (O'Brien and Goedecke 1988; Evans and Vivekanandan 1990; Draine and Flatau 1994; Aydin and Tang 1997). The accuracy of the DDA, the finite difference time domain method, and other numerical methods is limited mainly by the avail-

ability of adequate computer resources and target microphysical characteristics. In situ data collected with balloons or aircraft are limited to small sampling volumes that may not represent the characteristics of adjacent regions. In situ data is often unavailable for mixed-phase cloud regions or intense storms, such as those measured during MCTEX.

Backscatter and extinction cross sections for the spheres and crystals described above are calculated using the DDA. DDSCAT (V5a) FORTRAN code (Draine and Flatau 1996) was run on a Silicon Graphics Power Challenge with four R10K processors. Spherical particle models were compared with those calculated using Mie cross sections to verify the accuracy of the DDA models.

To obtain accurate DDA scattering computations: 1) the lattice spacing between dipoles, d, must be small compared to both the maximum particle dimension and radar wavelength and 2) the number of dipoles, N, must be sufficiently large to describe the target shape. Using the constraints described by Draine and Flatau (1996), these conditions are satisfied when

$$|n|\frac{2\pi}{\lambda}d \leq 1 \tag{A5}$$

and

$$N > \frac{4\pi}{3}|n|^3\left(\frac{2\pi a_{\text{eff}}}{\lambda}\right)^3. \tag{A6}$$

Here, a_{eff} is the radius for a sphere of volume equal to that of the model particle and n is the index of refraction. Given the maximum particle dimensions and particle density in Table A1, the model space dimensions are adjusted to ensure accuracy and optimize memory usage for each particle geometry. For spheres, a model space of $36 \times 36 \times 36$ produces errors of only a few percent at W band for diameters up to 18 mm for the Mitchell density function. Errors are less than 2% for median diameters as large as 10 mm.

REFERENCES

Ackerman, T., E. Clothiaux, R. Austin, M. Platt, S. Young, W. Ecklund, S. Sekelsky, and R. McIntosh, 1996: The Maritime Continent Thunderstorm Experiment: Cirrus anvil outflow, the Garden Point MCTEX research group. Preprints, *1996 Atmospheric Radiation Measurement (ARM) Program Science Team Meeting,* San Antonio, TX, U.S. Department of Energy, 13.

Atlas, D., S. Matrosov, A. Heymsfield, M. Chou, and D. Wolff, 1995: Radar and radiation properties of ice clouds. *J. Appl. Meteor.*, **34,** 2329–2345.

Auer, A., and D. Veal, 1970: The dimensions of ice crystals in natural clouds. *J. Atmos. Sci.,* **27,** 919–926.

Aydin, K., and T. Walsh, 1996: Computational study of millimeter wave scattering from bullet rosette type ice crystals. *Proc. 1996 Int. Geoscience and Remote Sensing Symp.,* Lincoln, NE, IEEE, 563–565.

——, and C. Tang, 1997: Millimeter wave radar scattering from model ice crystal distributions. *IEEE Trans. Geosci. Remote Sens.*, **35,** 140–146.

Bankert, R. L., 1994: Cloud classification of AVHRR imagery in maritime regions using a probabilistic neural network. *J. Appl. Meteor.,* **33,** 909–918.

Battan, L. J., 1973: *Radar Observation of the Atmosphere.* University of Chicago, 324 pp.

Bohren, C. F., and S. B. Singham, 1991: Backscattering by nonspherical particles: A review of methods and suggested new approaches. *J. Geophys. Res.,* **96** (D3), 5269–5277.

Brown, P., and P. Francis, 1995: Improved measurements of ice water content in cirrus using a total water probe. *J. Atmos. Oceanic Technol.* **12,** 410–414.

Carter, D., K. Gage, W. Ecklund, W. Angevine, P. Johnston, A. Riddle, J. Wilson, and C. Williams, 1995: Developments in UHF lower tropospheric wind profiling at NOAA's aeronomy laboratory. *Radio Sci.,* **30,** 977–1001.

Deirmendjian, D., 1969: *Electromagnetic Scattering on Spherical Polydispersions.* American Elsevier, 290 pp.

Draine, B., and P. Flatau, 1994: Discrete-dipole approximation for scattering calculations. *J. Opt. Soc. Amer.,* **11A,** 1491–1499.

——, and ——, 1996: User Guide to the discrete dipole approximation code DDSCAT Version 5a. Princeton Observatory Preprint POPe-695, Princeton University Observatory, Princeton University, Princeton, NJ, 39 pp. [Available from Princeton University Observatory, Princeton University, Princeton, NJ 08544-1001; available via anonymous ftp from astro.princeton.edu/draine/scat/ddscat/ver5a.]

Eccles, P. J., and D. Atlas, 1973: A dual-wavelength radar hail detector. *J. Appl. Meteor.* **12,** 847–856.

Ecklund, W., C. Williams, P. Johnston, and K. Gage, 1999: A 3-GHz profiler for precipitating cloud studies. *J. Atmos. Oceanic Technol.,* in press.

Evans, K. F., and J. Vivekanandan, 1990: Multiparameter radar and microwave radiative transfer modeling on nonspherical atmospheric ice particles. *IEEE Trans. Geosci. Remote Sens.,* **28,** 423–437.

Galloway, J., A. Pazmany, J. Mead, R. E. McIntosh, D. Leon, J. French, R. Kelly, and G. Vali, 1997: Detection of ice hydrometeor alignment using an airborne W-band polarimetric radar. *J. Atmos. Oceanic Technol.,* **14,** 3–12.

Gossard, E. E., 1994: Measurement of cloud droplet size spectra by Doppler radar. *J. Atmos. Oceanic Technol.,* **11,** 712–726.

Gunn, K., and J. S. Marshall, 1958: The distribution with size of aggregate snowflakes. *J. Meteor.,* **15,** 452–461.

Haykin, S., 1994: *Neural Networks: A Comprehensive Foundation.* MacMillan College Publishing, 696 pp.

Hendry, A., G. C. McCormick, and B. Barge, 1976: The degree of common orientation of hydrometeors observed by polarization diversity radars. *J. Appl. Meteor.,* **15,** 633–640.

Heymsfield, A., 1972: Ice crystal terminal velocities. *J. Atmos. Sci.,* **29,** 1348–1357.

Hobbs, P., S. Chang, and J. Locatelli, 1974: The dimensions and aggregation of ice crystals in natural clouds. *J. Geophys. Res.* **79,** 2199–2206.

Intrieri, J. M., G. L. Stephens, W. L. Eberhard, and T. Uttal, 1993: A method for determining cirrus cloud particle sizes using lidar and radar backscatter technique. *J. Appl. Meteor.,* **32,** 1074–1082.

Keenan, T., and Coauthors, 1994: Science Plan Maritime Continent Thunderstorm Experiment (MCTEX). BMRC Research Rep. 44, BMRC, Melbourne, Victoria, Australia, 61 pp. [Available from Bureau of Meteorology, BMRC, P.O. Box 1289k, Melbourne, Victoria 3001, Australia.]

Kosarev, A., and J. Mazin, 1991: An empirical model of the physical structure of upper layer clouds. *Atmos. Res.,* **26,** 213–228.

Lhermitte, R. M., 1987: Observations of stratiform rain with 94 GHz and S-band Doppler radar. Tech. Rep. AFGL-TR-0268, Air Force Geophysics Laboratory, Hanscom AFB, MA, 18 pp. [Available from Air Force Geophysics Laboratory, Air Force Systems Command, United States Air Force, Hanscom Air Force Base, MA 01731.]

——, 1988: Cloud and precipitation remote sensing at 94 GHz. *IEEE Trans. Geosci. Remote Sens.,* **26,** 207–216.
Locatelli, J., and P. Hobbs, 1974: Fall speeds and masses of solid precipitation particles. *J. Geophys. Res.,* **79,** 2185–2197.
Lohmeier, S. P., S. M. Sekelsky, J. M. Firda, G. A. Sadowy, and R. E. McIntosh, 1997: Classification of particles in stratiform clouds using the 33 and 95 GHz polarimetric cloud profiling radar system. *IEEE Trans. Geosci. Remote Sens.,* **35,** 256–270.
Magono, C., and T. Nakamura, 1965: Aerodynamic studies of falling snowflakes. *J. Meteor. Soc. Japan,* **43,** 139–147.
Marshall, J., and W. Palmer, 1948: The distribution of raindrops with size. *J. Meteor.,* **5,** 165–166.
Matrosov, S. Y., 1992: Radar reflectivity in snowfall. *IEEE Trans. Geosci. Remote Sens.,* **30,** 454–461.
——, 1993: Possibilities of cirrus particle sizing from dual-frequency radar measurements. *J. Geophys. Res.,* **98** (D11), 20 675–20 683.
——, J. B. Snider, and R. A. Kropfli, 1992: Estimation of ice cloud parameters from ground-based infrared radiometer and radar measurements. *J. Geophys. Res.,* **97** (D11), 11 567–11 574.
McFarquhar, G., and A. Heymsfield, 1996: Microphysical characteristics of three anvils sampled during the central equitorial Pacific experiment. *J. Atmos. Sci.,* **53,** 2401–2423.
Metcalf, J. I., 1995: Radar observations of changing orientations of hydrometeors in thunderstorms. *J. Appl. Meteor.,* **34,** 757–772.
Mitchell, D., R. Zhang, and R. Pitter, 1990: Mass–dimensional relationships for ice particles and the influence of riming on snowfall rates. *J. Appl. Meteor.,* **29,** 153–163.
Nemarich, J., R. J. Wellman, B. E. Gordon, D. R. Hutchins, G. A. Turner, and J. Lacombe, 1984: Attenuation and backscatter for snow and sleet at 96, 140 and 225 GHz. *Proc. Snow Symp. IV,* Hanover, NH, U.S. Army Cold Regions Research and Engineering Laboratory, 41–52.
O'Brien, S. G., and G. H. Goedecke, 1988: Scattering of millimeter waves by snow crystals and equivalent homogeneous symmetric particles. *Appl. Opt.,* **27,** 2439–2444.
Oguchi, T., 1983: Electromagnetic wave propagation and scattering in rain and other hydrometeors. *Proc. IEEE,* **71,** 1836–1844.
Platt, C., 1978: Lidar backscattering from horizontal ice crystal plates. *J. Appl. Meteor.,* **17,** 482–488.
Ray, P., 1972: Broadband complex refractive indices of ice and water. *Appl. Opt.,* **11,** 1836–1844.
Sassen, K., 1987a: Ice cloud content from radar reflectivity. *J. Climate Appl. Meteor.,* **26,** 1050–1053.
——, 1987b: Polarization and Brewster angle properties of light pillars. *J. Opt. Soc. Amer.,* **4A,** 570–580.
Sekelsky, S. M., and R. E. McIntosh, 1996: Cloud observations with a polarimetric 33 GHz and 95 GHz radar. *Meteor. Atmos. Phys.,* **58,** 123–140.
Sekhon, R. S., and R. C. Srivastava, 1970: Snow size spectra and radar reflectivity. *J. Atmos. Sci.,* **27,** 299–307.
Smith, P. L., 1984: Equivalent radar reflectivity factors for snow and ice particles. *J. Climate Appl. Meteor.,* **23,** 1258–1260.
Tang, C., and K. Aydin, 1995: Scattering from ice crystals at 94 and 220 GHz millimeter wave frequencies. *IEEE Trans. Geosci. Remote Sens.,* **33,** 93–99.
Thomason, J., A. Illingworth, and V. Marecal, 1995: Density and size distribution of aggregating snow particles inferred from coincident aircraft and radar observations. Preprints, *27th Conf. on Radar Meteorology,* Vail, CO, Amer. Meteor. Soc., 127–129.
Ulbrich, C. W., 1983: Natural variations in the analytical form of the raindrop size distribution. *J. Climate Appl. Meteor.,* **22,** 1764–1775.
Xiao, R., and V. Chandrasekar, 1997: Development of a neural network based algorithm for rainfall estimation from radar observables. *IEEE Trans. Geosci. Remote Sens.,* **35,** 160–171.
Zell, A., G. Mamier, and M. Vogt, 1995: Stuttgart Neural Network Simulator, Version 4.1: User manual. University of Stuttgart, Stuttgart, Germany, 312 pp. [Available from University of Stuttgart, SNNS Group Breitwiesenstrasse 20-22 Stuttgart, Germany 70565; available via anonymous ftp from ftp.informatik.uni-stuttgart.de/pub/SNNS.]